universe

MDPI

Article

Line-of-Sight Mass Estimator and the Masses of the Milky Way and Andromeda Galaxy

Danila Makarov [1], Dmitry Makarov [1,*], Kirill Kozyrev [1,2] and Noam Libeskind [3]

[1] Special Astrophysical Observatory, Russian Academy of Sciences, 369167 Nizhnij Arkhyz, Russia
[2] Institute of Physics, Kazan Federal University, 420008 Kazan, Russia
[3] Leibniz Institut für Astrophysik Potsdam (AIP), An der Sternwarte 16, D-14482 Potsdam, Germany
* Correspondence: dim@sao.ru

Abstract: The total mass of a galaxy group, such as the Milky Way (MW) and the Andromeda Galaxy (M 31), is typically determined from the kinematics of satellites within their virial zones. Bahcall and Tremaine (1981) proposed the v^2r estimator as an alternative to the virial theorem. In this work, we extend their approach by incorporating the three-dimensional spatial distribution of satellites within the system to improve the reliability and accuracy of galaxy mass estimates. Applying this method to a comprehensive dataset of local group satellites based on recent, high-precision distance measurements, we estimate the total mass of the MW to be $(7.9 \pm 2.3) \times 10^{11}\ M_\odot$ and that of M 31 to be $(15.5 \pm 3.4) \times 10^{11}\ M_\odot$. The effectiveness of the method is constrained by the precision of distance measurements, making it particularly well suited for the local group, but challenging to apply to more distant systems.

Keywords: local group; Andromeda Galaxy; Milky Way; dark matter

check for updates

Academic Editor: Andrea Lapi

Received: 12 March 2025
Revised: 25 April 2025
Accepted: 27 April 2025
Published: 30 April 2025

Citation: Makarov, D.; Makarov, D.; Kozyrev, K.; Libeskind, N. Line-of-Sight Mass Estimator and the Masses of the Milky Way and Andromeda Galaxy. *Universe* **2025**, *11*, 144. https://doi.org/10.3390/universe11050144

Copyright: © 2025 by the authors. Licensee MDPI, Basel, Switzerland. This article is an open access article distributed under the terms and conditions of the Creative Commons Attribution (CC BY) license (https://creativecommons.org/licenses/by/4.0/).

1. Introduction

Analyzing kinematics within virial zones remains the primary—and sometimes the only—available method for estimating the total mass of gravitating systems. To this end, various analogues of the virial theorem are used [1–3]. For distant systems, only line-of-sight velocities and the projected sky positions of galaxies are typically accessible through observations, leading to substantial uncertainties in mass estimates. Accounting for the three-dimensional distribution of satellites, derived from distance measurements, eliminates the uncertainty associated with sky projection and, consequently, may improve the reliability of mass estimates for nearby groups.

Over the past two decades, significant breakthroughs have been made in exploring the structure of the nearby Universe, thanks to the Hubble Space Telescope and advances in high-precision distance measurement techniques. For instance, according to the Color-Magnitude Diagram Catalog [4] of the Extragalactic Distances Database [5], the tip of the red giant branch (TRGB) distances have been measured for about 500 nearby galaxies with a median accuracy of 3.7%, covering scales up to 10 Mpc. As a result, we now have a detailed understanding of the three-dimensional distribution of satellites around giant Local Volume galaxies, particularly those surrounding the Milky Way (MW) and the Andromeda Galaxy (M 31).

In most nearby groups, the central galaxy dominates its system in both luminosity and mass. The aim of this paper is to develop a simple method, with a minimal number of free parameters, for the mass estimation of a massive galaxy, accounting for the three-dimensional distribution of its satellites. A simple model of a point mass surrounded

by test particles can be used for this purpose. This is exactly the case considered in the work of Bahcall and Tremaine [1]. Therefore, we extend their projection estimator method by incorporating the three-dimensional satellite distances and averaging the observed parameters over all possible orbits. Since the only remaining uncertainty is the projection of the satellite velocity onto the line of sight, we refer to this approach as the line-of-sight mass estimator. In addition, it is also necessary to investigate the applicability of the method to the study of nearby galaxy groups.

MW and M 31 serve as ideal case studies for testing this method. Modern sky surveys offer researchers access to a wealth of high-precision data, which, among other outcomes, have led to a remarkable increase in publications devoted to the mass estimates of the two dominant local group galaxies, using a variety of methods and tracers. As an example, we present several recent results that illustrate the diversity of approaches.

Modeling the rotation curve of a galaxy is a classical way to determine the parameters of its gravitational potential. In this way, Zhou et al. [6] constructed the circular velocity curve of the MW from 5 to 25 kpc using 54,000 luminous red giant branch stars. They determined the parameters of a model that included the bulge, thin, and thick disks, and a Navarro–Frenk–White dark halo [7], estimating the total mass of the Galaxy as $(8.5 \pm 1.2) \times 10^{11}\ M_\odot$ with a corresponding virial radius of 192 ± 9 kpc.

Globular clusters allow us to trace the Galactic gravitational potential to much larger distances—typically around 40 kpc and extending up to 100 kpc. Using Gaia Data Release 2, Vasiliev [8] determined the proper motions of nearly the entire known population of Milky Way globular clusters. By combining these with the distances and line-of-sight velocities, he analyzed their distribution in six-dimensional phase space. As a result, he derived the total enclosed mass to be $5.4^{+1.1}_{-0.8} \times 10^{11}\ M_\odot$ within 50 kpc, and $8.5^{+3.3}_{-2.0} \times 10^{11}\ M_\odot$ within 100 kpc. The extrapolated virial mass and radius are $12^{+15}_{-5} \times 10^{11}\ M_\odot$ and 280^{+80}_{-50} kpc, respectively.

Satellites are the only tracers that cover the entire virialized region of a group. In analyzing satellite kinematics, it is crucial to account for perturbations caused by the passage of a massive galaxy, such as the Large Magellanic Cloud (LMC), which can distort the satellite velocity distribution and bias the virial mass estimate. Kravtsov and Winney [9] developed a new robust halo mass estimator, $M \propto r_{\rm med}\sigma^3_{\rm 3D}$, calibrated using simulated MW-size halos. Based on this, they estimated the virial mass of the Milky Way to be $(9.96 \pm 1.45) \times 10^{11}\ M_\odot$.

The next level involves studying the deceleration of the Hubble flow due to the gravitational influence of the Local Group, allowing for mass estimates on scales of about 1 Mpc. For example, Karachentsev et al. [10] measured the radius of the zero-velocity surface to be $R_0 = 0.96 \pm 0.03$ Mpc, which corresponds to the total mass of $M_{\rm LG} = (19 \pm 2) \times 10^{11}\ M_\odot$. However, this topic is beyond the scope of the present study and will be addressed in future work.

The examples provided above only represent a tiny fraction of the studies devoted to understanding the structure of the Milky Way. They demonstrate the potential of testing the new method using various approaches. In addition, the new method will provide one more independent estimate of the mass to the collection.

This article is organized as follows. Section 2 briefly describes the projection mass method. Section 3 is devoted to the line-of-sight mass estimator. Comparison with numerical models is performed in Section 4. Its application to the mass estimation of our Galaxy and the Andromeda Galaxy is discussed in Section 5. We conclude in Section 6.

2. Projection Mass Method

By considering the motion of test particles around a point mass, Bahcall and Tremaine [1] showed that, due to projection effects, the mass of a galaxy group, as given by the virial theorem, $M_{\rm vir}$, is statistically one of the following:

1. *Biased*, meaning that the average of $M_{\rm vir}$ estimates for the same group is not necessarily equal to the true mass for a finite number of particles, N;
2. *Inefficient* with a large variance;
3. *Inconsistent* in some cases, meaning that $M_{\rm vir}$ does not converge to the true mass as $N \to \infty$.

The main reason for the inefficiency of the virial mass estimate is the uncertainty introduced by the projection factor in the distances between galaxies. However, even without considering projection effects, $M_{\rm vir}$ remains ineffective, as nearby particles contribute more than distant ones to both the estimate of kinetic energy (as the sum of squared velocities, $\sum_i v_i^2$) and to the estimate of potential energy (as the harmonic mean of distances, $\sum_i 1/r_i^2$). Since both distant and nearby particles provide the same information about the central mass, it is evident that the virial estimate, $M_{\rm vir}$, does not effectively utilize all available information.

As an alternative to the virial theorem, Bahcall and Tremaine [1] propose to use the so-called projection mass estimate, which is directly based on the observed values

$$GM_{\rm p} = a v_{\rm los}^2 r_{\rm p}, \tag{1}$$

where $v_{\rm los}$ is the line-of-sight velocity of the particle with respect to the central body, and $r_{\rm p}$ is its projected separation. This method treats test particles at all distances equally, since on average $\langle v_{\rm los}^2 r_{\rm p} \rangle = \text{const}$. The correction coefficient, a, is determined by averaging over all possible particle trajectories in the system. As a result, for the typical case of observing a distant group with a dominant massive galaxy, Bahcall and Tremaine [1] derived

$$GM_{\rm p} = \frac{32}{\pi(3 - 2\langle e^2 \rangle)} \langle v_{\rm los}^2 r_{\rm p} \rangle. \tag{2}$$

To obtain a realistic estimate of the mass, one must make an assumption about the orbits of the particles. The most natural assumption is that the velocity distribution is isotropic, with an eccentricity of $\langle e^2 \rangle = 1/2$. In this case, the projected mass estimator, $M_{\rm I}$, becomes

$$GM_{\rm I} = \frac{16}{\pi} \langle v_{\rm los}^2 r_{\rm p} \rangle, \tag{3}$$

with the variance of

$$\mathrm{Var}\Big(\langle GM_{\rm I} \rangle\Big) = \frac{1}{N}\left(\frac{128}{5\pi^2} - 1\right) \langle GM_{\rm I} \rangle^2, \tag{4}$$

where N is the number of test particles.

3. Line-of-Sight Mass Method

Our goal is to derive a correction factor, a, for the mass estimator, based on an expression of the form

$$GM_{\rm los} = a v_{\rm los}^2 r, \tag{5}$$

where $v_{\rm los}$ is the line-of-sight velocity of the test particle, and r is the spatial separation from the central body. Hereafter, we adopt the notation and approach used in the work of Bahcall

and Tremaine [1]. The average of any quantity $\xi(\boldsymbol{r}, \boldsymbol{v})$ can be obtained by integrating over the distribution function $f(\boldsymbol{r}, \boldsymbol{v})$ of a spherically symmetric gravitating system

$$\langle \xi \rangle = A \int_0^\infty r^2 dr \int_0^\pi \sin\Theta \, d\Theta \int_0^\infty v_\perp \, dv_\perp \int_{-\infty}^\infty dv_r \int_0^{2\pi} \xi f \, d\phi'. \tag{6}$$

Here, Θ is the polar angle of the radius vector $\boldsymbol{r}$ in a spherical coordinate system, with the polar axis directed toward the observer; ϕ' is the azimuthal angle of the velocity vector $\boldsymbol{v}$ in a cylindrical system, where the z axis is aligned along the radius vector; v_r and $v_\perp$ are the components of the velocity vector directed along and perpendicular to the radius vector, respectively; and A is the normalization coefficient.

According to Jeans's theorem, any steady-state solution of the collisionless Boltzmann equation depends on the phase–space coordinates only through the integrals of motion. For a spherically symmetric system of test particles, the distribution function is determined by the energy, $E = GM/r - v^2/2$, and the square of the angular momentum, $J^2 = r^2 v_\perp^2$. For a particle with the specific values of energy, E_0, and angular momentum, J_0, it can be expressed using the Dirac delta function[1]:

$$\begin{aligned} f(\boldsymbol{r}, \boldsymbol{v}) = f(E, J) &= \delta(E - E_0)\, \delta(J^2 - J_0^2) \\ &= \delta(GM/r - v^2/2 - E_0)\, \delta(r^2 v_\perp^2 - J_0^2). \end{aligned} \tag{7}$$

Given the property of the delta function,

$$\delta(f(x)) = \sum_i \frac{\delta(x - x_i)}{|f'(x_i)|},$$

where x_i are roots of the function $f(x)$, the Equation (6) is transformed to

$$\begin{aligned} \langle \xi \rangle &= A \textstyle\int_0^\infty r^2 dr \int_0^\pi \sin\Theta \, d\Theta \int_0^\infty v_\perp \, dv_\perp \int_{-\infty}^\infty dv_r \\ &\quad \times \textstyle\int_0^{2\pi} \xi \delta(GM/r - v^2/2 - E_0) \delta(r^2 v_\perp^2 - J_0^2) \, d\phi' \\ &= A \textstyle\int_{r_{\min}}^{r_{\max}} r^2 dr \int_0^\pi \sin\Theta \, d\Theta \int_0^{2\pi} \xi \frac{2}{|v_r|} \frac{1}{|2r^2|} \, d\phi' \\ &= A \textstyle\int_{r_{\min}}^{r_{\max}} dr \int_0^\pi \sin\Theta \, d\Theta \int_0^{2\pi} \frac{\xi}{|v_r|} \, d\phi' \end{aligned} \tag{8}$$

where

$$v_\perp^2 = \frac{J_0^2}{r^2} = \frac{(GM)^2}{2E_0}(1 - e^2)\frac{1}{r^2} \tag{9}$$

$$\begin{aligned} v_r^2 &= 2\tfrac{GM}{r} - \tfrac{J_0^2}{r^2} - 2E_0 \\ &= 2\tfrac{GM}{r} - \tfrac{(GM)^2}{2E_0}(1 - e^2)\tfrac{1}{r^2} - 2E_0, \end{aligned} \tag{10}$$

and it is taken into account that the maximum angular momentum for a given energy E_0 is $J_{\max} = GM/(2E_0)^{1/2}$, and the eccentricity is defined as $e^2 = 1 - (J/J_{\max})^2$. The integration limits are defined by the relations $v_r(r_{\min}) = v_r(r_{\max}) = 0$ and are equal to

$$r_{\min} = \frac{GM}{2E_0}(1 - e) \tag{11}$$

$$r_{\max} = \frac{GM}{2E_0}(1 + e). \tag{12}$$

Bahcall and Tremaine [1] determined the normalization coefficient A by considering the condition $\langle 1 \rangle = 1$

$$A = \left(4\pi \int_{r_{\min}}^{r_{\max}} \frac{dr}{|v_r|} \right)^{-1} = \frac{(2E_0)^{3/2}}{4\pi^2 GM}. \tag{13}$$

Using the dimensionless variable $x = \frac{2E_0}{GM} r$, Equations (8)–(10) simplify to:

$$\begin{aligned} r &= \tfrac{GM}{2E_0} x \\ v_\perp^2 &= 2E_0 \tfrac{1-e^2}{x^2} \\ v_r^2 &= 2E_0 \tfrac{e^2-(x-1)^2}{x^2} \\ \langle \xi \rangle &= \tfrac{1}{4\pi^2} \int_{1-e}^{1+e} \tfrac{x\,dx}{\sqrt{e^2-(x-1)^2}} \int_0^{\pi} \sin\Theta\, d\Theta \int_0^{2\pi} \xi\, d\phi'. \end{aligned} \tag{14}$$

It is clear from this that, although we considered the distribution function at the arbitrary fixed energy, E_0, of a test particle, the average of observable values of the form $\langle v^2 r \rangle \propto 2E_0 \frac{GM}{2E_0} = GM$ depends only on the mass of the central body, not on E_0. This allows us to determine the mass regardless of the particle energy distribution. However, orbital eccentricity still plays a role.

As noted by Bahcall and Tremaine [1], the variance of the mass estimator of the form given in Equation (5) is well defined and can be determined in a similar way. Let us define the value

$$(GM_{\rm los})^2 = b(v_{\rm los}^2 r)^2. \tag{15}$$

Then, the variance is

$$\begin{aligned} \mathrm{Var}(GM_{\rm los}) &= \mathrm{Var}(a v_{\rm los}^2 r) = a^2 \mathrm{Var}(v_{\rm los}^2 r) \\ &= a^2 \left(\langle (v_{\rm los}^2 r)^2 \rangle - \langle v_{\rm los}^2 r \rangle^2 \right) = a^2 \left(\tfrac{(GM)^2}{b} - \left(\tfrac{GM}{a} \right)^2 \right) \\ &= \left(\tfrac{a^2}{b} - 1 \right) (GM_{\rm los})^2. \end{aligned} \tag{16}$$

Accordingly, the variance of the mean $\langle GM \rangle$ is equal to

$$\mathrm{Var}\Big(\langle GM_{\rm los} \rangle \Big) = \frac{1}{N} \left(\frac{a^2}{b} - 1 \right) \langle GM_{\rm los} \rangle^2, \tag{17}$$

where N is the number of the test particles.

Our case of finding the average $\langle v_{\rm los}^2 r \rangle$ actually involves two scenarios: one where the observer sits near the center of the group (as in the case of the Milky Way), and another where the observer views the system from the side (as in the case with all other nearby groups of galaxies).

3.1. Milky Way Case

In the case of the Milky Way group, we are essentially at the center of the system with respect to the distribution of satellites. As a consequence, the line of sight nearly coincides with the radial coordinate, allowing us to approximate $v_{\rm los} \approx v_r$ with good accuracy. Thus,

$$\begin{aligned} \langle v_{\rm los}^2 r \rangle = \langle v_r^2 r \rangle &= 4\pi A \int_{r_{\rm min}}^{r_{\rm max}} r |v_r|\, dr \\ &= \tfrac{GM}{\pi} \int_{1-e}^{1+e} \sqrt{e^2-(x-1)^2}\, dx = \tfrac{GM}{2} \langle e^2 \rangle. \end{aligned} \tag{18}$$

Consequently, the line-of-sight mass estimator for the Milky Way is

$$GM_{\rm los} = \frac{2}{\langle e^2 \rangle} \langle v_r^2 r \rangle. \tag{19}$$

To estimate the variance, we obtain the value

$$\langle (v_{\rm los}^2 r)^2 \rangle = (GM_{\rm los})^2 \left(\frac{3}{2} e^2 - 1 + (1-e^2)^{3/2} \right), \tag{20}$$

which yields the variance of the mass estimate for our Galaxy equal to

$$\mathrm{Var}\Big(\langle GM_{\rm los}\rangle\Big) = \frac{1}{N}\frac{4}{\langle e^2\rangle}\left(\frac{3}{2}\langle e^2\rangle - 1 + (1-\langle e^2\rangle)^{3/2}\right). \tag{21}$$

In the case of an isotropic velocity distribution, where $\langle e^2\rangle = \frac{1}{2}$, the line-of-sight mass estimator and its variance become

$$GM_{\rm I} = 4\langle v_r^2 r\rangle \tag{22}$$

$$\mathrm{Var}\Big(\langle GM_{\rm I}\rangle\Big) = \frac{4(\sqrt{2}-1)}{N}\langle GM_{\rm I}\rangle^2 \approx \frac{1.657}{N}\langle GM_{\rm I}\rangle^2. \tag{23}$$

3.2. Nearby Group Case

Consider the case where the observer is at a sufficient distance from the group. Assume that the three-dimensional distribution and line-of-sight velocities of the satellites are known from observations. This case corresponds to nearby galaxy groups in the Local Volume, where high-precision distances have been measured for many galaxies. The line-of-sight velocity can be represented as $v_{\rm los} = v_r\cos\Theta - v_\perp \sin\phi' \sin\Theta$. Equation (8) is transformed into the form

$$\begin{aligned}\langle v_{\rm los}^2 r\rangle &= \tfrac{4\pi A}{3}\int_{r_{\rm min}}^{r_{\rm max}} r v_r\left(1+\tfrac{v_\perp^2}{v_r^2}\right)dr\\ &= \tfrac{GM}{3\pi}\int_{1-e}^{1+e}\tfrac{1-(x-1)^2}{\sqrt{e^2-(x-1)^2}}\,dx\\ &= \tfrac{GM}{6}\big(2-\langle e^2\rangle\big).\end{aligned} \tag{24}$$

Similarly, for the mean square, we obtain the following expression:

$$\langle (v_{\rm los}^2 r)^2\rangle = \frac{(GM)^2}{10}\Big(2-\langle e^2\rangle\Big). \tag{25}$$

The corresponding mass estimator and its variance are

$$GM_{\rm los} = \frac{6}{2-\langle e^2\rangle}\langle v_{\rm los}^2 r\rangle \tag{26}$$

$$\mathrm{Var}\Big(\langle GM_{\rm los}\rangle\Big) = \frac{1}{N}\left(\frac{36}{10(2-\langle e^2\rangle)}-1\right)\langle GM\rangle^2. \tag{27}$$

For an isotropic distribution over orbits $\langle e^2\rangle = \frac{1}{2}$, we obtain

$$GM_{\rm I} = 4\langle v_{\rm los}^2 r\rangle \tag{28}$$

$$\mathrm{Var}\Big(\langle GM_{\rm I}\rangle\Big) = \frac{7}{5N}\langle GM_{\rm I}\rangle^2 = \frac{1.4}{N}\langle GM_{\rm I}\rangle^2. \tag{29}$$

Note that, despite the fundamental difference in the general expressions for the mass of the Milky Way (Equation (18)) and the nearby group (Equation (24)), the correction factors for the isotropic case, as given in Equations (22) and (28), coincide surprisingly.

3.3. Additional Notes

Watkins et al. [3] presented an entire family of estimators of the form $M \propto \langle v^2 r^\alpha\rangle$, similar to the projected mass method initially introduced by Bahcall and Tremaine [1] and later expanded by Heisler et al. [2]. The estimators are derived from the solutions of Jeans's equation, assuming that the tracers follow a power-law density distribution and move within a gravitational potential that also takes a power-law form.

It is worth noting that, despite significant progress in discovering the satellites of the Milky Way and the Andromeda Galaxy, their spatial distribution remains strongly affected by selection effects. This effect becomes even more pronounced for more distant systems. As Watkins et al. [3] point out, this can alter the observed power-law slope of the tracer number density and, consequently, lead to a bias in the mass estimate. Although our approach is simpler, it bypasses this problem by averaging the observables $v_{\rm los}^2 r$ over all possible orbits, independent of the radial distribution of satellites, whether measured or model-based. This may be particularly useful for distant systems, where the number of known satellites is very limited. In addition, this approach allowed us to derive explicit expressions for the error in the mass estimation.

4. Comparison with Cosmological Simulations

To test the applicability of the method, we applied it to the high-resolution environmental simulations of the immediate area (HESTIA, [11]). It is a set of cosmological models specifically designed to simulate the Local Group of galaxies. These constrained dark-matter and magneto-hydrodynamic simulations are based on the AREPO code [12]. The initial conditions are derived from the peculiar velocities of the nearby galaxies in the CosmicFlows-2 survey [13], using a reverse Zeldovich approximation [14]. Baryonic physics follows the AURIGA galaxy formation model [15].

The simulations include a high-resolution region of 3–5 Mpc around the Local Group analog, where galaxies similar to the Milky Way and Andromeda Galaxy are formed. In this area, a mass resolution of $m_{\rm dm} = 1.2 \times 10^6\ M_\odot$ and a gas particle resolution of $m_{\rm gas} = 1.8 \times 10^5\ M_\odot$ are achieved. These simulated galaxies match observations in terms of various physical and morphological properties, making them useful for studying the role of the surrounding environment in terms of galactic evolution [11]. Thanks to the technique of constrained simulations, the Local Group analog is surrounded by structures that closely resemble real-world environments, such as the Virgo-like cluster, local void, and local sheet.

HESTIA offers three high-resolution models of the Local Group. We are primarily interested in the positions of the halos in space and their peculiar velocity vectors at $z = 0$. All relevant quantities are expressed in simulation units and can be rescaled to different cosmological parameters if necessary. The top panel of Figure 1 presents the radial velocity of the surrounding halos as a function of distance for the second most massive halo—the MW analog—in the `17_11` HESTIA run. Its total mass is $M_{\rm tot} = 13.3 \times 10^{11}\ M_\odot$, while the largest halo, which is the analog of M 31, has a total mass of $M_{\rm tot} = 15.6 \times 10^{11}\ M_\odot$. The first thing that catches the eye is the significant difference in the velocity–distance distribution of satellites compared to that observed around the Milky Way (see Figure 3 in Section 5.1). The HESTIA 'satellites' (the halos with stars) within 50 kpc in the `17_11` run exhibit a very low line-of-sight velocity dispersion, $\sigma_V = 36.3\ {\rm km\,s^{-1}}$, compared to $\sigma_V = 113.3\ {\rm km\,s^{-1}}$ for more distant halos. This reflects the effects of dynamical friction and the reorganization of the orbits of the nearest halos into more circular ones, as well as the impact of the smaller mass enclosed within this radius. Additionally, below 30–40 kpc, selection effects in halo identification become significant, resulting in a noticeable deficiency of halos at short distances from the central body. This pattern is typical for all central massive halos in the HESTIA runs.

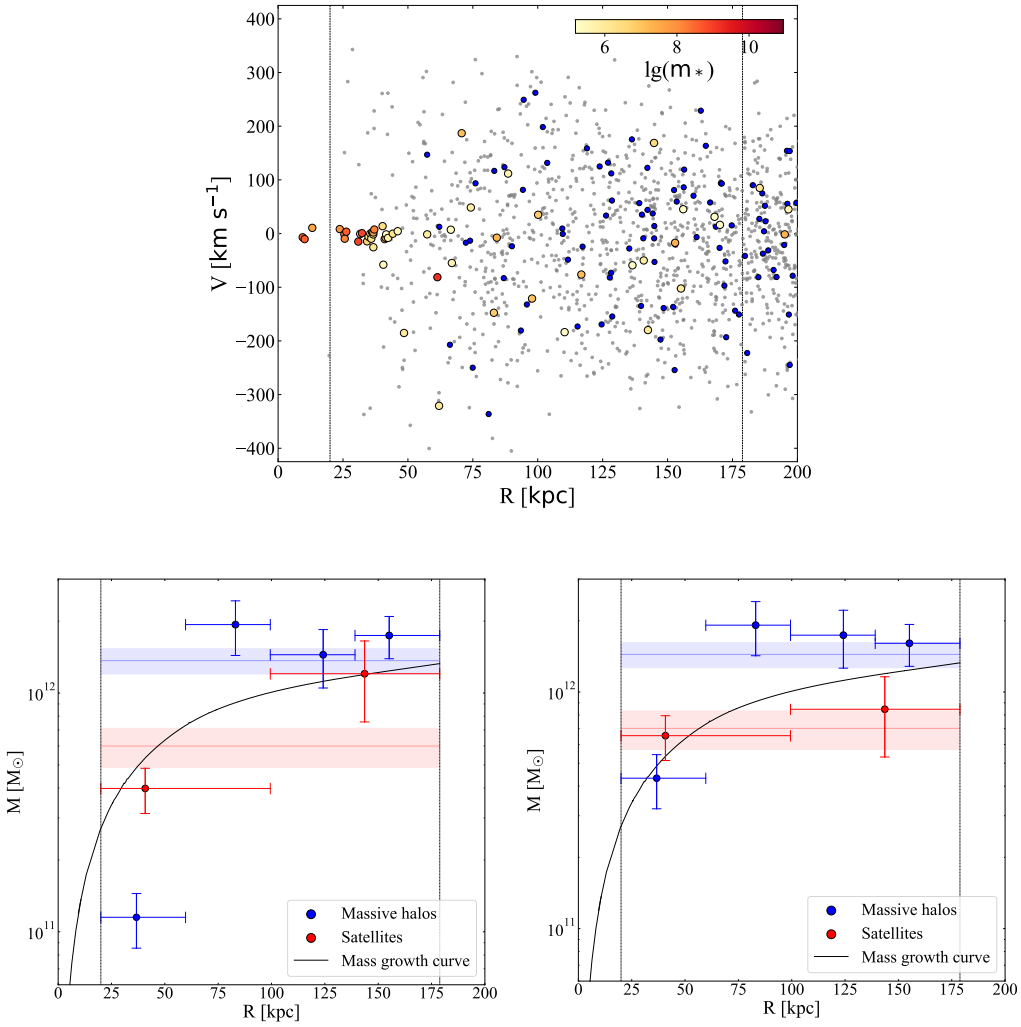


Figure 1. (**Top panel:**) Radial velocity–distance diagram for all halos surrounding the MW analog in the HESTIA `17_11` simulation. Gray dots represent the distribution of low-mass dark matter halos. Blue dots correspond to massive halos with $m_{\rm dm} > 4.3 \times 10^7\ M_\odot$. Large colored dots indicate satellite-like halos with stellar masses greater than $m_* > 1.5 \times 10^5\ M_\odot$. Vertical lines denote the selected region beyond 20 kpc and within the virial radius of 178.9 kpc. (**Bottom left panel:**) Mass estimates based on observations from the center of the massive halo, within the radial range of $[20, 178.9]$ kpc. Red dots show the masses obtained for two satellite subgroups, while the red line represents the result based on all satellites within the specified range. Similarly, four blue dots indicate the masses' estimates from 112 massive halos grouped into four equal radial intervals, while the blue line shows the result for the full sample. The solid black line depicts the cumulative mass profile $M(< r)$, as extracted directly from the simulation. (**Bottom right panel:**) Same as the left panel, but from the viewpoint of the nearest massive halo, imitating observations of M 31.

To mimic real observations, we placed an observer in the center of one of these massive halos and calculated the line-of-sight velocities of all surrounding halos based on their positions and peculiar velocities. We focus on virial zones around the two most massive halos: the MW and M 31 analogs. Their virial radii vary from 143 to 189 kpc, depending on the mass of the central halo. We also exclude from consideration all halos located within 20 kpc of the main massive halo. This decision is motivated by two factors: first, the difficulty of reliably identifying such objects in cosmological simulations due to the high-density region of the central massive halo; and second, observational evidence that satellites at these distances are likely embedded within the central galaxy body, where they

are subject to strong tidal forces and eventual accretion. As a result, we obtain two sets of data: one for observing the satellites of the given halo, and another for observing the satellites of the next massive halo. In total, we obtain six datasets for each scenario. In our tests, we apply the line-of-sight mass estimator, assuming isotropic orbits (Section 3), to both samples. The first consists of 'satellites'—halos containing star particles with stellar mass $m_* > 1.5 \times 10^5\ M_\odot$—and typically includes around 30 objects. The second sample of heavy halos includes all halos with $m_{\rm dm} > 4.3 \times 10^7\ M_\odot$, corresponding to the lower mass threshold for halos capable of hosting star formation, and typically comprises around 100 test particles. We compared the estimated mass with the total mass of all halos enclosed within the virial radius. The results are summarized in Table 1. The bottom left and right panels of Figure 1 compare the mass estimates with the mass growth curve within the virial radius of the MW analog in the HESTIA simulation `17_11`. The left panel represents the point of view of the internal observer, while the right panel reflects the view from the center of the neighboring massive halo.

Table 1. Statistics on the tests of mass estimation of the MW and M 31 analogs using the HESTIA simulations.

Sample	$\left\langle \frac{M_{\rm I}}{\sum M_{\rm halo}} \right\rangle$		σ	Median
Observations from the outside (the case of M 31)				
Heavy halos	1.054	$\pm$0.042	0.103	1.055
Satellites	0.858	$\pm$0.157	0.384	0.848
Observations from the inside (the case of MW)				
Heavy halos	1.022	$\pm$0.048	0.116	1.047
Satellites	0.704	$\pm$0.129	0.315	0.625

It is important to note that the masses derived from the samples at different distances follow the halo mass growth curve in the simulations. Because of the limited number of 'satellites', mass estimates based on this sample exhibit significant scatter. In contrast, including all massive halos significantly improves the statistics, reduces the scatter to 10–12%, and enhances the robustness of the mass estimates. As shown in Table 1, the average ratio of the estimated mass to the true value is statistically consistent with unity within the 1-sigma uncertainty. This supports the conclusion that the proposed approach is suitable for estimating the mass of virialized systems and provides realistic measurements.

5. Application to the Local Group of Galaxies

The Local Group of galaxies requires no special introduction. It is a fairly isolated system, bound within a radius of approximately 1 Mpc. The nearest comparable galaxy groups are located at a distance of 3–4 Mpc [16]. The Local Group is based on two giant spiral galaxies separated by 780 kpc, the Milky Way and the Andromeda Galaxy, which are similar to each other in many ways. These giants are surrounded by rich suites of satellites that extend up to 300 kpc. Only about a dozen dwarf galaxies are known in the Local Group outside the virial zones of the MW and M 31. Thanks to modern deep optical surveys and systematic searches, our knowledge of the Local Group population has expanded dramatically. The list of satellites is growing with new members all the time. This allows one to trace their population to extremely low luminosity, which is technically inaccessible for more distant galaxy groups. The recently discovered galaxy Ursa Major III [17] has a luminosity of $M_V = +2.2$ mag, corresponding to a stellar mass of only 16 $M_\odot$. The subsystems of the MW and M 31 satellites do not overlap, allowing them to be studied independently, without considering complex interactions. Various methods and subsystems are used to estimate the mass, from the motion of stars and gas in

the galaxies themselves, to the study of the kinematics of globular clusters and satellites, the timing argument for the orbiting of the MW and M 31, and the Hubble flow braking at the Local Group boundary (see recent reviews by [18–20]). All this allows us to trace the distribution of both baryonic and dark matter in the Local Group, spanning a scale from a few kiloparsecs to approximately one megaparsec. There is a consensus that the M 31 is a slightly more massive galaxy than MW [3,10,21], although the mass estimates for both galaxies vary widely, sometimes leading to the opposite conclusion [22]. New mass estimates for the MW and M 31 remain an important goal in the study of these galaxies and the Local Group as a whole.

The sample of the MW and M 31 satellites was compiled based on the latest version of the Local Volume galaxy database [23], taking into account recent work on studying cosmic flows around nearby massive galaxies [24], measuring proper motions of MW satellites [25,26], estimating distances from RR Lyrae variables [27], recent galaxy discoveries (for instance [28], HyperLeda [29] and NED databases, and many other works). Members of the MW and M 31 groups with compiled distances and heliocentric line-of-sight velocities are presented in Appendix A and Appendix B, respectively.

Figure 2 shows the three-dimensional distribution of satellites of our Galaxy (left panel) and the Andromeda Galaxy (right panel) in Supergalactic coordinates (the Z coordinate is indicated by color). The famous satellite planes are clearly visible around both galaxies [30]. Also, the M 31 satellites demonstrate a well-known skew toward our Galaxy [31].

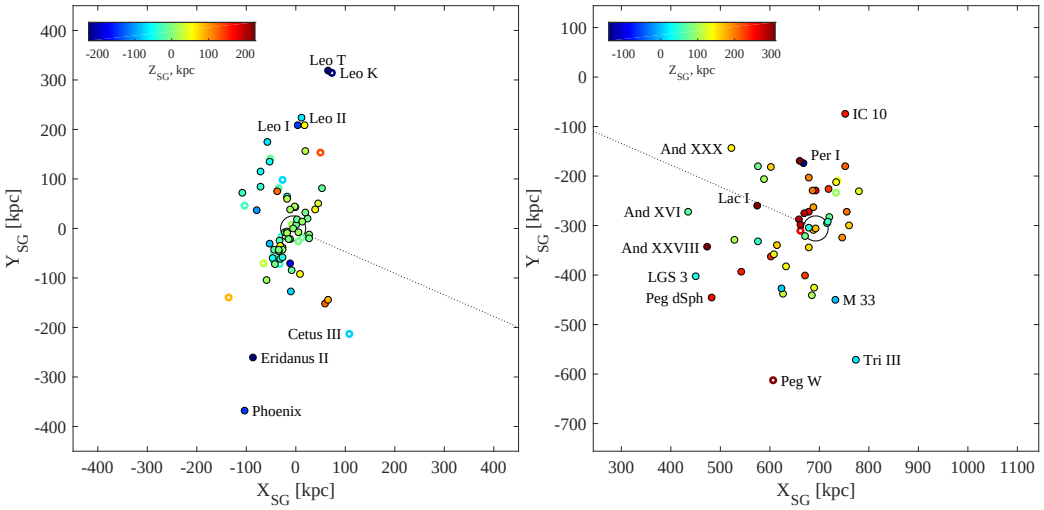


Figure 2. Three-dimensional-distribution of galaxies within 450 kpc from MW (**left panel**) and M 31 (**right panel**) in Cartesian supergalactic coordinates. The Z axis is indicated by color. Galaxies with an unknown line-of-sight velocity are shown by open-colored circles. The dotted line connects MW and M 31. Satellites located further than 220 kpc from the central galaxy are labeled.

5.1. Milky Way

Thanks to the Gaia mission [32], the proper motions of most of the satellites of our Galaxy have been measured, which unambiguously allows us to determine all six components of the satellite position in phase space. This information is actively used to refine the structure of our Galaxy, to estimate its total mass, and to analyze the features of satellite orbits. It should be emphasized that the line-of-sight velocities of satellites are measured an order of magnitude more accurately than their proper motions. Therefore, an independent mass estimate based on simple line-of-sight velocities remains extremely important.

Moreover, even a simple analysis of the line-of-sight velocity distribution can reveal unexpected and interesting effects. Recently, Makarov et al. [33] discovered that the dipole component of the line-of-sight velocity field shows an unexpectedly large amplitude of

226 ± 50 km s^{-1} of the bulk motion of nearby satellites at distances less than 100 kpc. This anomaly is caused by only eight galaxies (crossed out with red crosses in the left panel of Figure 3), which include the LMC and three galaxies from its escort. Numerical simulations demonstrate that this velocity pattern is consistent with the assumption of the first flyby of the massive LMC around our Galaxy and the perturbation it creates in the motion of the MW satellites. This example shows the importance of a careful selection of "the test particles" for kinematic analysis. Objects on the first flyby do not have time to virialize and therefore should be excluded from consideration when estimating the total mass of the system.

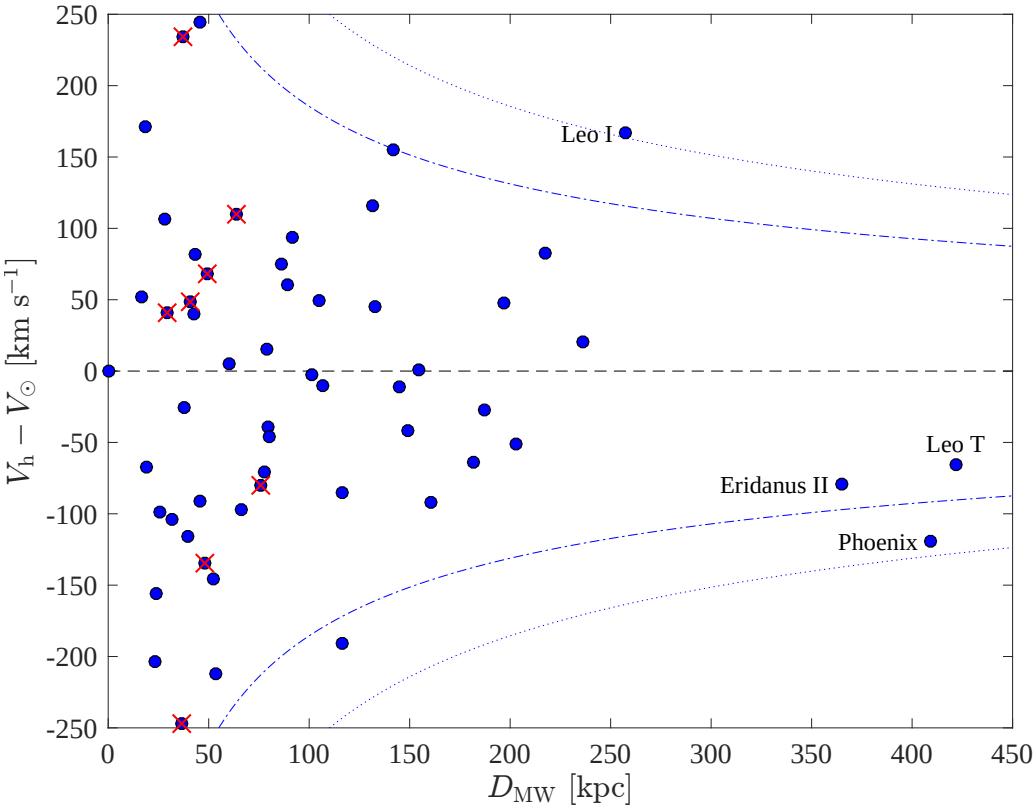


Figure 3. The velocity–distance distribution of the nearest galaxies relative to the center of our Galaxy. The eight satellites that cause the greatest disturbance in the behavior of the solar apex are marked with red crossmarks. The circular and escape velocities of the point mass $8 \times 10^{11}\ M_\odot$ are shown by the dashed and dotted lines, respectively.

At present, there are 67 known satellites of our Galaxy within the 260 kpc region. As can be seen in Figure 3, there is a clear separation between the well-randomized MW satellites up to distances of 260 kpc, indicating the extension of the virial zone, and three galaxies with systematic negative velocity at a distance of 400 kpc, which are probably just entering the MW halo for the first time. Thus, we limited the analysis area to a distance of 260 kpc.

As shown by Makarov et al. [33], after excluding eight objects that most strongly distort the behavior of the solar apex, the observed collective motion of the remaining satellites is consistent within errors with the motion of the Sun in our Galaxy. Thus, in further analysis, the observed line-of-sight velocities were simply corrected for the solar velocity vector of $(9.5, 250.7, 8.56)$ km s^{-1} [34] with respect to the Galactic center, determined from the proper motion of Sgr A* of $(-6.411 \pm 0.008, -0.219 \pm 0.007)$ mas yr^{-1} in Galactic coordinates [35] and the distance of $8249 \pm 9 \pm 45$ pc to the central supermassive black hole [36].

The case of Leo I deserves special attention. As can be seen in Figure 3, this most distant satellite near the border of the virial zone has an extremely high line-of-sight velocity. The inclusion of Leo I (just one galaxy) in the analysis leads to a dramatic 33% increase in the total MW mass [3]. Currently, it is not entirely clear whether the orbit of Leo I is elliptic or hyperbolic [37]. Nevertheless, proper motion measurements indicate that Leo I is likely bound to the Milky Way [38], but it is on an extremely elongated orbit with an eccentricity of $0.79^{+0.10}_{-0.09}$ [26]. Nevertheless, we prefer to exclude it from the analysis, since it is a drastic outliers from the general behavior of the satellites. Its orbit also obviously does not satisfy the isotropy condition that we use in the following analysis. Moreover, there is evidence of tidal stripping in this galaxy [39], indicating its violent prehistory, and as a consequence, it cannot be considered as a simple test particle.

Based on the results obtained in Section 3.1 and assuming an isotropic distribution of satellite orbits, we estimate the MW mass using different subsamples of satellites. Figure 4 presents the behavior of the running line-of-sight mass estimated from 20 satellite sequences for the case of all galaxies (dashed line) and after excluding the eight members of the group with a large collective motion (solid blue line). As you can see, the exclusion of these eight galaxies does not radically change the mass estimates, but the trend of mass growth with distance appears more clearly. This behavior is a natural consequence of the density distribution in the dark matter halos surrounding galaxies. However, because of the small statistics, errors and random fluctuations turn out to be quite large.

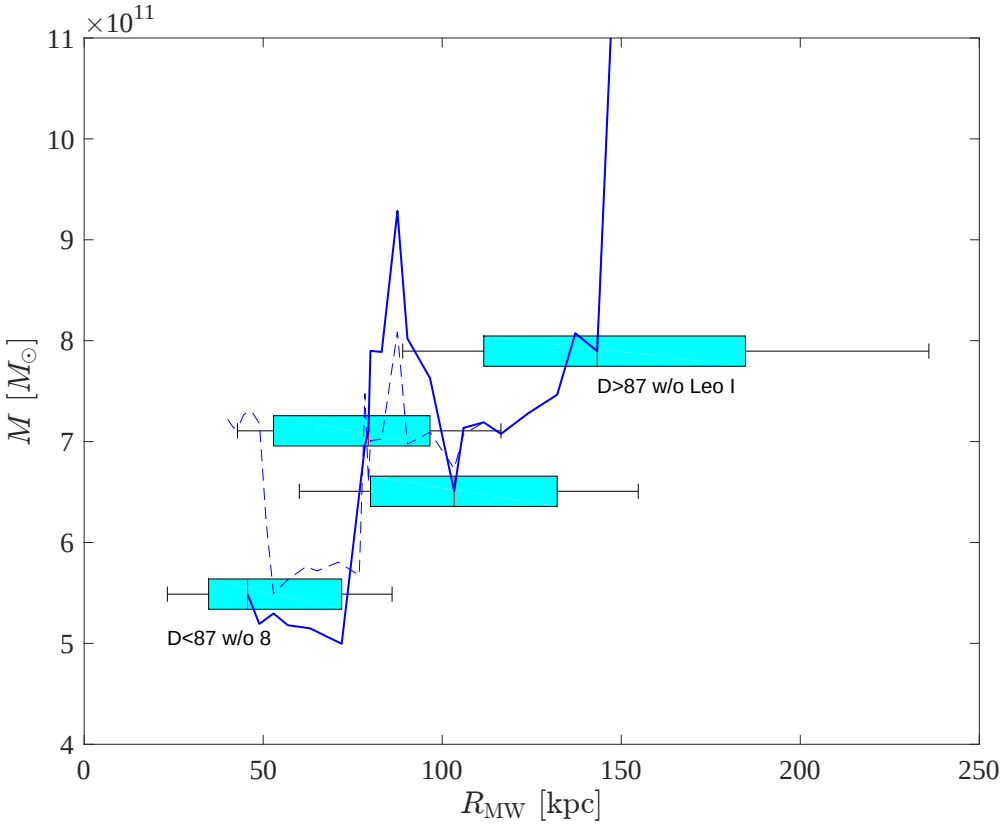


Figure 4. Mass estimates of the Milky Way based on subsamples of 20 satellites. Cyan boxplots represent the measured values and illustrate the nonparametric statistics of the distance distribution for the satellites used. Specifically, the whiskers indicate the minimum and maximum distances within the sample, the box denotes the first and third quartiles, and the median is shown by a vertical line segment within the box. The first box corresponds to the '$D < 86$ kpc w/o 8' sample, while the fourth represents the '$D < 86$ kpc w/o Leo I' sample (see Table 2). The solid blue line indicates the running mass based on subsamples of 20 satellites, excluding eight galaxies. The dashed line shows the running mass for the full sample.

Table 2. Summary of the MW mass estimates.

Sample	**Range [kpc]**		#	$M_{\rm I}$ [$\times 10^{11}\ M_\odot$]
All	23	257	49	8.1 ± 1.5
w/o Leo I	23	236	48	6.9 ± 1.3
w/o 8	23	257	41	8.1 ± 1.6
w/o 8 and Leo I	23	236	40	6.7 ± 1.4
$D < 86$ kpc	23	86	28	6.2 ± 1.5
w/o 8	23	86	20	5.5 ± 1.6
$D > 86$ kpc	89	257	21	10.7 ± 3.0
w/o Leo I	89	236	20	7.9 ± 2.3

The results are summarized in Table 2. It gives the range of galactocentric distances of satellites, the sample size, and the corresponding mass estimate, $M_{\rm I}$, assuming isotropic orbits. The distance of 86 kpc is chosen on the basis that, at large distances, the motion of the satellites is well randomized and does not show significant collective motions relative to the Galactic center [33], and this boundary also divides the sample of satellites into equal parts. It is evident that Leo I gives a significant increase in the total mass of the Galaxy, which is especially noticeable in the case of external satellites, where its contribution increases the mass estimate by 35%. Based on this analysis, we estimate the mass of the Galaxy within 86 kpc to be in the range of [5.5–6.2] $\times\ 10^{11}\ M_\odot$ with an uncertainty of $\pm 1.5 \times 10^{11}\ M_\odot$, and a total mass within 240 kpc to be $(7.9 \pm 2.3) \times 10^{11}\ M_\odot$.

The diversity and abundance of new observational data have triggered a surge in estimates of the mass of our Galaxy. Over the past decade, four reviews on the dynamics and mass of MW have been published. Bland-Hawthorn and Gerhard [40], in their review "The Galaxy in Context", obtained an average of individual mass estimates equal to $(11 \pm 3) \times 10^{11}\ M_\odot$. Based on a compilation of 47 individual mass measurements obtained using seven different methodologies, Wang et al. [18] concluded that the virial mass of our Galaxy is still determined with a scatter of a factor of two and is likely to be confined between 5×10^{11} and $20 \times 10^{11}\ M_\odot$. In a recent review, Bobylev and Baykova [19] used 20 published measurements of the total mass within a radius of 200 kpc. They determined a mean value of $(8.8 \pm 0.6) \times 10^{11}\ M_\odot$ with a standard deviation of $2.4 \times 10^{11}\ M_\odot$. Hunt and Vasiliev [41] claimed that the MW mass estimates converge around $10^{12}\ M_\odot$ with an uncertainty of about 20–30%.

Building upon the compilations by Wang et al. [18] and Bobylev and Baykova [19], we supplemented their data with 12 new measurements published after 2020. Table A3 presents a list of 37 mass estimates for our Galaxy within at least 200 kpc, conducted over the past 15 years. A comparison of our measurements with data from the literature is shown in Figure 5. The measurements are grouped by the classes of methods used. Our mass estimate is indicated by a vertical line, with its uncertainty represented by the shaded gray region. It can be seen that our value of $(7.9 \pm 2.3) \times 10^{11}\ M_\odot$ within 240 kpc is in good agreement with numerous estimates reported by other authors. Only measurements based on the phase–space distribution function systematically yield higher masses. As noted in the review by Wang et al. [18], this may be due to a mismatch between the model and real distribution functions, as well as a violation of the steady-state assumption caused by phase–space correlations and the influence of LMC. After excluding the phase–space distribution function methods and considering 28 individual measurements, we derive a mean value of $(10.3 \pm 0.6) \times 10^{11}\ M_\odot$ with a standard deviation of $3.0 \times 10^{11}\ M_\odot$, and a median value of $9.5 \times 10^{11}\ M_\odot$, which lies within 1 sigma of our estimate and closely matches the case where Leo I is included into consideration.

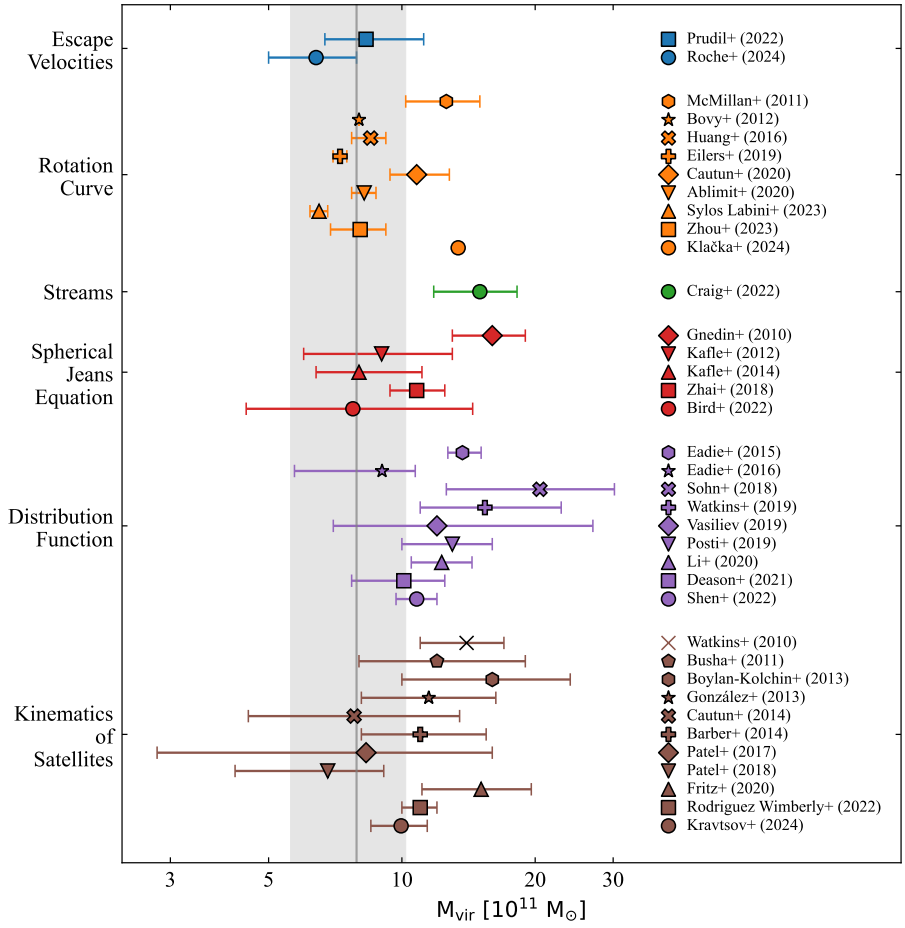


Figure 5. Comparison of our estimate of the MW mass with recent measurements obtained by different authors: Prudil et al. [42], Roche et al. [43], McMillan [44], Bovy et al. [45], Huang et al. [46], Eilers et al. [47], Cautun et al. [48], Ablimit et al. [49], Sylos Labini et al. [50], Zhou et al. [6], Klačka et al. [51], Craig et al. [52], Gnedin et al. [53], Kafle et al. [54], Kafle et al. [55], Zhai et al. [56], Bird et al. [57], Eadie et al. [58], Eadie and Harris [59], Sohn et al. [60], Watkins et al. [61], Vasiliev [8], Posti and Helmi [62], Li et al. [63], Deason et al. [64], Shen et al. [65], Watkins et al. [3], Busha et al. [66], Boylan-Kolchin et al. [38], González et al. [67], Cautun et al. [68], Barber et al. [69], Patel et al. [70], Patel et al. [71], Fritz et al. [72], Rodriguez Wimberly et al. [73], Kravtsov and Winney [9].

5.2. Andromeda Galaxy

The sky distribution of the 50 known neighbors of M 31 within 500 kpc of it is shown in Figure 6. Unlike the MW satellites, the proper motions in the Andromeda group are only known for a few galaxies: M 31 [74,75], M 33 [74,76], NGC 185, NGC 147, IC 10 [76], and And III [77]. However, the tangential velocity is determined with large errors and the significance of such measurements rarely exceeds four sigma. Therefore, to estimate the M 31 mass from the satellite motions, we must still rely only on their line-of-sight velocities.

The transverse velocity of the Andromeda Galaxy relative to our Galaxy also remains highly controversial (see Figure 6 in [75]). Salomon et al. [75] concluded that the approach of these two giant galaxies is radial. The correction of the observed velocity of M 31 for the solar motion in the Galaxy gives an approach velocity equal to -109 km s^{-1}. Unfortunately, the fairly compact location of the M 31 satellites in the sky leaves no chance to estimate the tangential velocity of the system using only line-of-sight velocities. We can only test the velocity component toward M 31. The average line-of-sight velocity of the M 31 satellite system within 200 kpc is -105 ± 20 km s^{-1}, which is almost identical to the velocity of the central galaxy. Beyond 200 kpc, the average velocity of the satellites diverges from that of

M 31, reaching $\Delta V \approx 35$ km s^{-1}, under the influence of M 33, its satellites And XXII and Tri III, and NGC 185. Therefore, for further analysis, we assume a head-on approach of our Galaxy and the Andromeda Galaxy with $V = -109$ km s^{-1}.

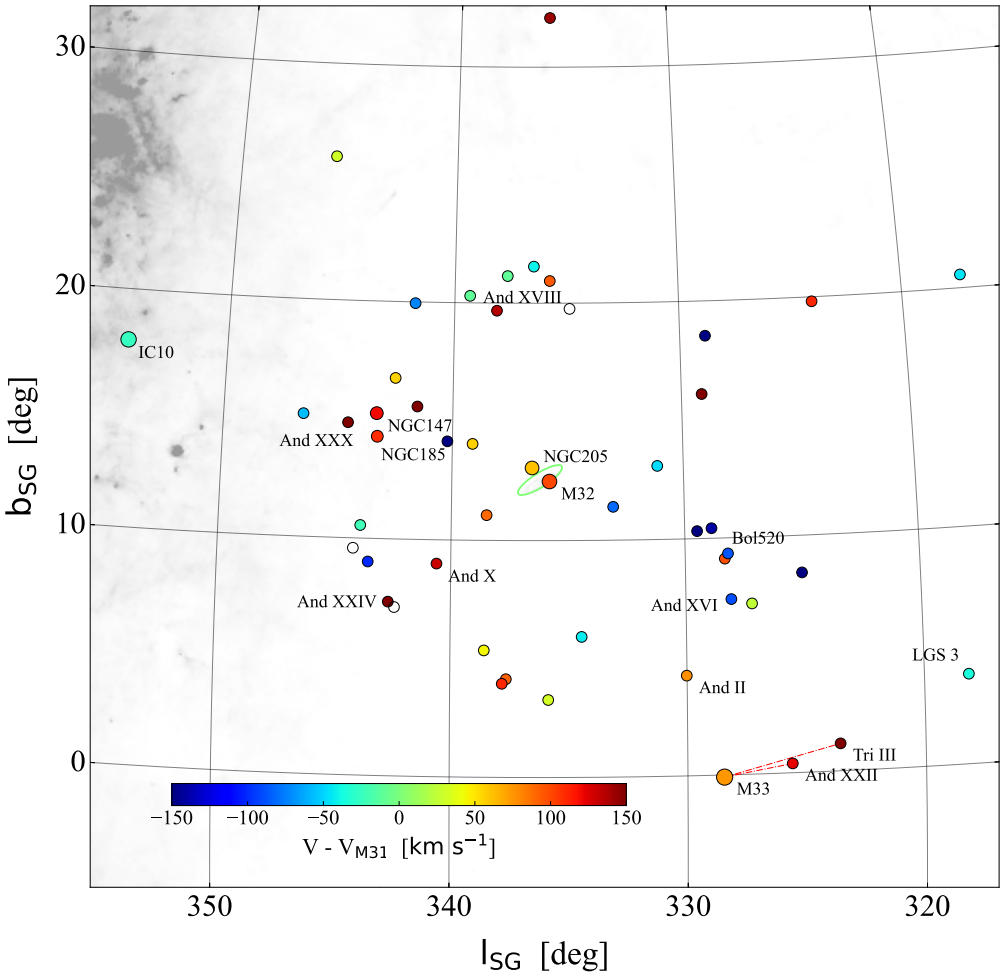


Figure 6. Distribution of the M 31 satellites in the sky in the Aitoff projection. M 31 is shown by a central ellipse. The color reflects the velocity difference relative to the central galaxy. The open dots mark galaxies with unknown line-of-sight velocities. The IRAS interstellar extinction map is given by gray clouds.

We estimate the total mass of the Andromeda Galaxy using the line-of-sight mass estimator assuming the isotropy of the orbits for the case of observing the system from the outside (Section 3.2). The results for different satellite subsamples are summarized in Table 3. In addition to the sample size (#), the velocity dispersion (σ_V), and the line-of-sight mass ($M_{\rm l}$), it also provides the line-of-sight mass ($M_{\rm l}^c$) corrected for the distance errors (see Section 5.3), and the mass obtained by the classical projected mass method ($M_{\rm l}^p$) proposed by Bahcall and Tremaine [1]. The description of the subsamples is given below.

As in the case of our Galaxy, the sample of M 31 satellites for mass determination requires some careful consideration. From the total list of 45 satellites around the Andromeda Galaxy within 300 kpc, we excluded all objects with unknown, questionable, or imprecise distance measurements because they could be a source of large systematic errors. Among them are eight objects from the Pan-Andromeda Archaeological Survey (PAndAS) without distance measurements. We also excluded all objects, whose distance errors are greater than 5%, namely Tri III (6.4%), probably satellite of M 33 [78]; a globular cluster Bol 520 (9.6%); IC 10 (5.7%) and And XXVII (5.7%), which reside in the region of high MW extinction. This sample is designated as '*D* and *cz*' in Table 3.

The Andromeda group has its own LMC analog. As shown by Patel et al. [79], M 33 is located near the apocenter of its first flyby around the Andromeda Galaxy. A plume of neutral hydrogen stretches along its trajectory. Therefore, we excluded from consideration M 33 with its suit of And XXII and Tri III[2] as not satisfying the requirement of isotropy of their orbits and virialization in the system. This sample is labeled as 'w/o 2' because it excludes two galaxies. For a similar reason, we do not include in consideration And XVIII at a distance of $1.33^{+0.06}_{-0.09}$ Mpc [80], which is located beyond the Andromeda Galaxy at a distance of 579 kpc and has not yet reached its virial zone. And XXX has an extremely high line-of-sight velocity $V = 159.6$ km s^{-1} relative to Andromeda, so in addition to the M 33 subgroup, we also excluded it from the analysis, as it could significantly distort the data. We call the sample 'w/o 3'.

We believe that the latter sample provides the most realistic estimate of the mass. Thus, our final sample contains 30 satellites within 300 kpc of M 31. Their distribution is characterized by the standard deviation of the line-of-sight velocity $\sigma_V = 112.7$ km s^{-1} and the average distance of $\langle r \rangle = 138$ kpc from the Andromeda Galaxy. Using the line-of-sight velocity method for nearby groups (Section 3.2), we estimate the total mass of M 31 as equal to $M_{\rm I} = (17.0 \pm 3.7) \times 10^{11}\ M_\odot$. As in the case of our Galaxy, the running mass and subsamples of nearby and more distant satellites show a trend in mass on the scale from 100 to 200–300 kpc (Figure 7).

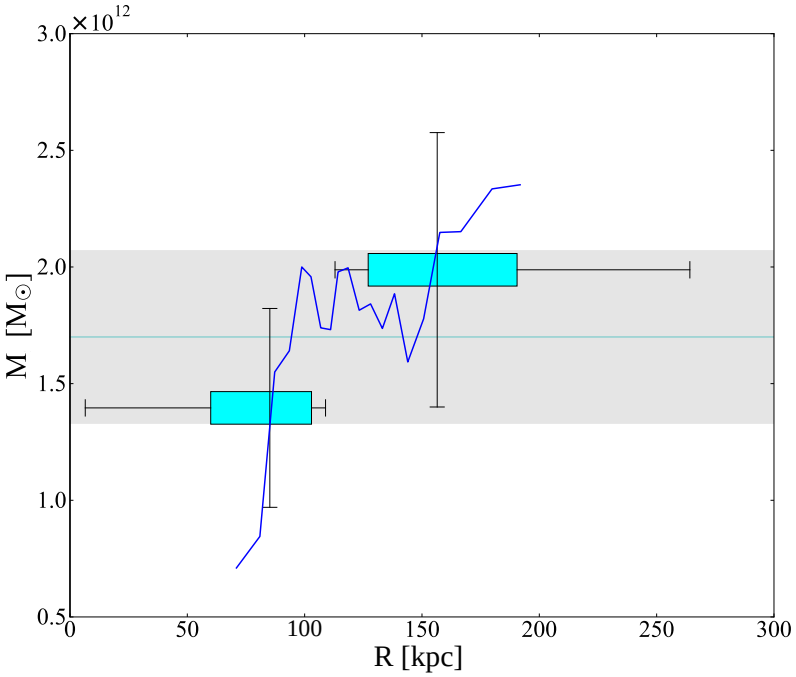


Figure 7. Resulted mass estimate of the Andromeda Galaxy as a function of distance. Two boxes correspond with both near and distant subsamples, each containing 15 satellites. The meaning of the boxplot is the same as in Figure 4. The total mass estimate $M = (17.0 \pm 3.7) \times 10^{11}\ M_\odot$ (cyan line) with its error (gray filling) is provided. The solid blue line shows the running mass for the entire sample.

It would be useful to compare this result with the classical approach based on the use of projected distances and line-of-sight velocities only. Using the same list of satellites, the projected mass method [1] gives a very close mass estimate of $M^p_{\rm I} = (17.4 \pm 4.0) \times 10^{11}\ M_\odot$, but with worse accuracy. However, it also allows us to include objects in the analysis without precise distance measurements and improve accuracy through statistics. Within a *projected* radius of 300 kpc from M 31, there are 47 galaxies with known velocities. This sample is labeled '*cz*' in Table 3. Based on this, we obtain a projected mass of

$M_{\rm I}^{p} = (22.7 \pm 4.2) \times 10^{11}\ M_{\odot}$. It can be seen that the accuracy is still lower than in our approach. This indicates the importance of knowing the distribution of satellites in space for a more accurate estimate of the galaxy mass.

Table 3. Summary of the M 31 mass estimates.

Sample	#	σ_V	$M_{\rm I}$	$M_{\rm I}^{c}$	$M_{\rm I}^{p}$
		km s^{-1}		$\times 10^{11}\ M_{\odot}$	
cz	47	121.1			22.7 ± 4.2
D and cz	33	114.1	18.5 ± 3.8	16.9 ± 3.5	21.7 ± 4.8
w/o 2 †	31	113.6	18.5 ± 3.9	16.9 ± 3.6	19.5 ± 4.4
w/o 3 ‡	30	112.7	17.0 ± 3.7	15.5 ± 3.4	17.4 ± 4.0

† excluding M 33 subgroup. ‡ excluding M 33 subgroup and And XXX.

5.3. Influence of the Distance Measurement Errors

The previous result was obtained under the assumption that we know the galaxy distances with absolute precision. Unfortunately, random errors in distance measurements lead to a systematic bias in the measured average separation of the satellites from the central galaxy and to a fictitious stretching of the system along the line of sight. As a result, we will overestimate the value of $v^2 r$, and as a consequence, the mass of the galaxy group. This effect can be especially significant when distance errors become comparable to the characteristic size of the system.

The typical accuracy of distance measurements in the near Universe is 3–4%. For the satellites of our Galaxy, this corresponds to a typical distance error of the order of a few kpc, which is negligible compared to the virial radius of the Milky Way. In the case of the Andromeda Galaxy, the situation is worse. At the distance of M 31, the typical error is 20–30 kpc, which is in the order of 10% of its virial radius.

To estimate the contribution of this systematic uncertainty to the mass of M 31, we apply the Monte Carlo method, which allows us to simulate distance measurements and the propagation of errors in a controlled manner. Assuming a Gaussian distribution of distance modulus errors, we randomly vary the measured distance modulus according to its measurement accuracy for all galaxies in the group including M 31 itself. The resulting modulii are then converted into linear distances in the standard way. All this leads to an asymmetric shift of galaxies along a line of sight relative to their original position. The mass estimate is made using exactly the same procedure as for the real galaxy group. Based on 100,000 random generations, we find that the observed distance errors lead to an effective overestimation of the mass by 9.7% with a standard deviation of 3%. As a result, for our final sample of 30 satellites, we obtain a corrected M 31 mass of $M_{\rm I}^{c} = (15.5 \pm 3.4) \times 10^{11}\ M_{\odot}$, where the error takes into account the small spread introduced by distance measurement errors.

On the one hand, the Andromeda Galaxy is easier to observe than the Milky Way, because we can see it from the outside. However, its significantly greater distance imposes certain observational limitations. Among other factors, this is reflected in the smaller number of studies that focus on the M 31 mass estimate. During the same period since 2010, we have compiled only 13 measurements of the total mass within 200 kpc, which is three times less than the number of estimates available for the Milky Way. We added only three new measurements to the review by Bhattacharya [20]. The list is presented in Table A4. As illustrated in Figure 8, our value $M_{\rm I}^{c} = (15.5 \pm 3.4) \times 10^{11}\ M_{\odot}$, indicated by a vertical line with a shaded region representing its uncertainty, is in excellent agreement with 13 recent measurements of the M 31 mass within 200 kpc. The mean of the data from

the literature is $(15.8 \pm 1.4) \times 10^{11}\ M_\odot$ with a standard deviation of $5.1 \times 10^{11}\ M_\odot$, and a median of $14.0 \times 10^{11}\ M_\odot$.

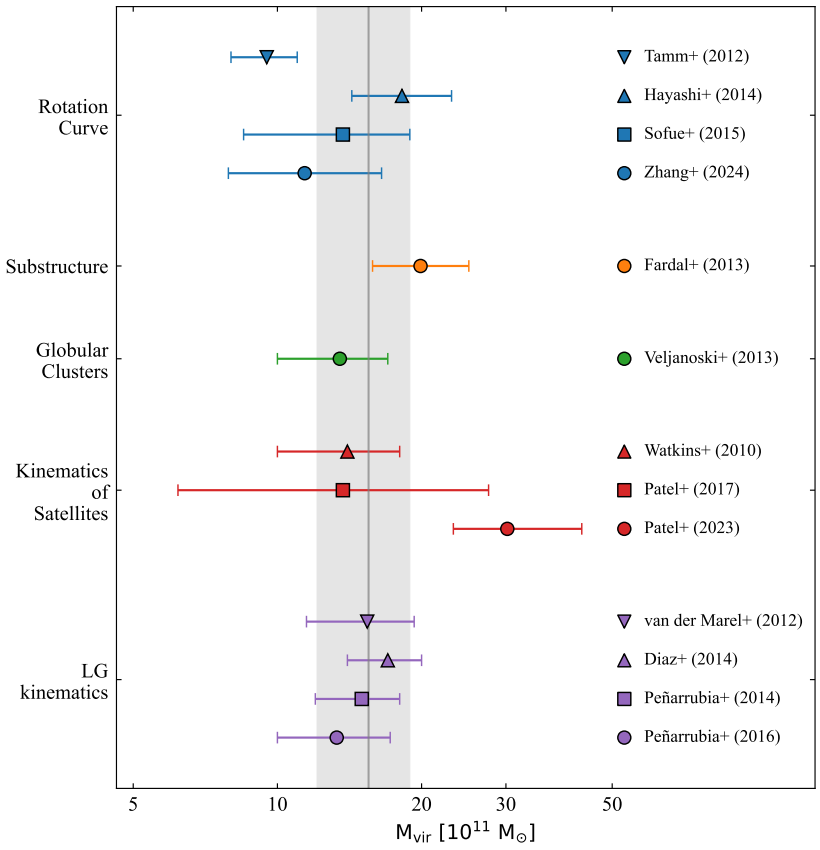


Figure 8. Comparison of our M 31 mass estimate (gray line) with the recently published mass measurements on the scale of 200 kpc using different methods. The compilation contains the following works: Tamm et al. [81], Hayashi and Chiba [82], Sofue [83], Zhang et al. [84], Fardal et al. [85], Veljanoski et al. [86], Watkins et al. [3], Patel et al. [87], Patel and Mandel [76], van der Marel et al. [88], Diaz et al. [89], Peñarrubia et al. [22], Peñarrubia et al. [90].

6. Discussion and Conclusions

We have developed a method for the mass estimation of groups with a dominant central galaxy, based on the $v^2 r$ estimator proposed by Bahcall and Tremaine [1], for the case of a known three-dimensional distribution of satellites in the system. This situation is realized in the nearby Universe, where high-precision distances for a large number of galaxies are available. Since the only unaccounted uncertainty in this case is related to the projection of the three-dimensional velocity onto the line of sight, we call this approach the line-of-sight mass estimator. As with the original projected-mass methodology, this approach requires an assumption about the nature of the satellite orbits in the system, which is expressed in terms of the mean square of the eccentricity $\langle e^2 \rangle$. We considered two cases: observations from the central galaxy (the case of the Milky Way and its satellites) and observations from outside the system. Despite the significant difference in the observation conditions, which is reflected in Equations (18) and (24), in the case of isotropic orbits, $\langle e^2 \rangle = 1/2$, the correction factor for both cases turned out to be the same and equal to 4 (Equations (22) and (28)). This coefficient differs from the naively expected correction of 3 for the case of a random projection of the velocity vector.

The comparison with numerical cosmological simulations confirmed the applicability of the method and showed good agreement with the true mass of the systems under the

assumption of the isotropic distribution of satellite orbits. In addition, this methodology allows us to trace the distribution of the mass of the system with distance.

Unfortunately, measurement errors in distance can lead to significant bias in the mass estimate. Since the distance errors increase with distance, the applicability of the method outside the Local Group is severely limited and requires a more sophisticated Bayesian approach and a joint consideration of the assumed distribution of satellites and their velocities to obtain more reliable determination.

The application of this methodology to the Local Group allowed us to estimate the masses of the Milky Way and the Andromeda Galaxy assuming an isotropic distribution of satellite orbits.

We estimate the total mass of our Galaxy on a scale of 240 kpc of $M_{\rm MW} = (7.9 \pm 2.3) \times 10^{11}\ M_\odot$. This value is in good agreement with recent measurements by other authors. The mean of 28 individual measurements performed since 2010 is $(10.3 \pm 0.6) \times 10^{11}\ M_\odot$ with a standard deviation of $3.0 \times 10^{11}\ M_\odot$, and a median value of $9.5 \times 10^{11}\ M_\odot$. Similar values have been reported in recent reviews. Bland-Hawthorn and Gerhard [40] obtained an average of individual mass estimates equal to $(11 \pm 3) \times 10^{11}\ M_\odot$. Wang et al. [18] concluded that the mass of our Galaxy is known with an uncertainty of a factor of two and is constrained within the range of 5×10^{11} and $20 \times 10^{11}\ M_\odot$. Bobylev and Baykova [19] derived a mean of $(8.8 \pm 0.6) \times 10^{11}\ M_\odot$, and a standard deviation of $2.4 \times 10^{11}\ M_\odot$, using a compilation of 20 measurements from the literature.

A significantly larger mass of our Galaxy of $(10.7 \pm 3.0) \times 10^{11}\ M_\odot$ is obtained when Leo I is included in the consideration. Its contribution outweighs all other satellites and increases the total mass by 35%. Measurements of its proper motion [26,38] indicate that Leo I is in an extremely elongated orbit with an eccentricity of $\sim$0.8. Taking this effect into account should slightly reduce the contribution of Leo I compared to the other satellites, but in any case, the impact remains significant. Thus, improving the accuracy of 3D velocity measurements and clarifying the orbital parameters of Leo I is extremely important for understanding the halo structure of our Galaxy and estimating its total mass.

We estimate the total mass of M 31 of $M = (15.5 \pm 3.4) \times 10^{11}\ M_\odot$ within a radius of 300 kpc. This value is also in excellent agreement with recent measurements. We supplemented the compilation by Bhattacharya [20] with three of the most recent measurements. The average of the Andromeda Galaxy mass derived from publications over the past 15 years is $(15.8 \pm 1.4) \times 10^{11}\ M_\odot$ with a scatter of $5.1 \times 10^{11}\ M_\odot$.

Thus, the measurement of the total mass of the two main galaxies of the Local Group by their satellite kinematics indicates that the M 31 is twice as massive as MW, $M_{\rm M31}/M_{\rm MW} = 2.0 \pm 0.7$. The similar ratio of $M_{\rm M31}/M_{\rm MW} = 1.75^{+0.54}_{-0.28}$ is obtained by Carlesi et al. [21] using a supervised machine learning algorithm on a cosmological simulation within the standard ΛCDM model and applying it to the distance and velocity distribution of the MW and M 31 satellites. However, it should be noted that the Hubble flow outside the virial radii of MW and M 31 indicates that the Local Group barycenter is located approximately midway between these galaxies. Karachentsev et al. [10] estimated the MW to M 31 mass ratio of $M_{\rm M31}/M_{\rm MW} \simeq 4/5$. Unfortunately, the errors in determining the masses remain large enough to speak of a statistically significant difference between these values.

Author Contributions: Conceptualization, D.M. (Dmitry Makarov); Methodology, D.M. (Danila Makarov) and D.M. (Dmitry Makarov); Validation, N.L.; Formal analysis, D.M. (Danila Makarov), K.K., and N.L.; Investigation, D.M. (Danila Makarov), D.M. (Dmitry Makarov), and K.K.; Resources, N.L.; Writing—original draft, D.M. (Danila Makarov), D.M. (Dmitry Makarov), K.K. and N.L.; Supervision, D.M. (Dmitry Makarov). All authors have read and agreed to the published version of the manuscript.

Funding: This work was supported by the Russian Science Foundation grant No. 24-12-00277.

Data Availability Statement: The original contributions presented in this study are included in the article material. Further inquiries can be directed to the corresponding author.

Acknowledgments: The authors thank Lidia Makarova for her valuable comments. We acknowledge the usage of the HyperLeda database[3] [29]. This research has made use of the NASA/IPAC Extragalactic Database (NED), which is funded by the National Aeronautics and Space Administration and operated by the California Institute of Technology. This research has made use of the Astrophysics Data System, funded by NASA under Cooperative Agreement 80NSSC21M00561.

Conflicts of Interest: The authors declare no conflicts of interest.

Appendix A. List of Satellites of the Milky Way

Table A1. Known satellites of the Milky Way galaxy.

Name	J2000	$(m-M)_0$			Method	D		V_h		
		mag				kpc		km s^{-1}		
Tucana IV	000255.2−605100	18.41	±0.19	[91]	TRGB	48.1	±4.4	15.9	$^{+1.8}_{-1.7}$	[25]
SMC	005238.0−724801	18.99	±0.05	[25]	Cep	62.8	±1.5	158	±4	[92]
Sculptor	010009.4−334233	19.67	±0.14	[25]	TRGB	85.9	±5.7	111.4	±0.1	[93]
Cetus II	011752.8−172512	17.10	±0.10	[94]	CMD	26.3	±1.2			
DELVE 2	015505.3−681511	19.26	±0.10	[95]	HB	71.1	±3.4			
Cetus III	020519.4−041612	22.00	$^{+0.20}_{-0.10}$	[25]	HB	251	$^{+24}_{-12}$			
Triangulum II	021317.4+361042	17.27	±0.11	[96]	CMD	28.4	±1.5	−381.70	±1.10	[25]
Segue 2	021916.0+201031	17.70	±0.10	[25]	TRGB	34.7	±1.6	−40.20	±0.90	[26]
Eridanus III	022245.5−521701	19.70	±0.15	[25]	HB	87.1	±6.2			
DES J0225+0304	022542.4+030410	16.88	$^{+0.06}_{-0.05}$	[97]	CMD	23.8	$^{+0.7}_{-0.6}$			
Hydrus I	022933.4−784128	17.20	±0.04	[25]	TRGB	27.5	±0.5	80.4	±0.6	[25]
Fornax	023954.7−343133	20.84	±0.18	[25]	TRGB	147	±13	55.2	±0.1	[93]
Horologium I	025531.7−540708	19.50	±0.20	[25]	HB	79.4	±7.7	112.8	$^{+2.5}_{-2.6}$	[25]
Horologium II	031632.1−500105	19.46	±0.20	[25]	HB	78.0	±7.5	168.7	$^{+12.9}_{-12.6}$	[25]
Reticulum II	033542.1−540257	17.40	±0.15	[25]	HB	30.2	±2.2	64.7	$^{+1.3}_{-0.8}$	[25]
Reticulum III	034526.4−602700	19.81	±0.31	[25]	CMD	92	±14	274.2	$^{+7.5}_{-7.4}$	[25]
Pictor I	044347.4−501659	20.30	±0.15	[25]	HB	115	±8			
LMC	052334.6−694522	18.50	±0.13	[98]	Cep	50.1	±3.1	278	±2	[99]
Columba I	053125.7−275727	21.31	±0.11	[96]	BHB	183	±10	153.7	$^{+5}_{-4.8}$	[25]
Carina	064136.7−505758	20.11	±0.13	[25]	TRGB	105	±7	222.9	±0.1	[25]
Pictor II	064443.2−595360	18.30	$^{+0.12}_{-0.15}$	[25]	HB	45.7	$^{+2.6}_{-3.3}$			
Carina II	073625.6−560003	17.79	±0.05	[25]	HB	36.1	±0.8	477.2	±1.2	[25]
Carina III	073831.2−560601	17.22	±0.10	[25]	HB	27.8	±1.3	284.6	$^{+3.4}_{-3.1}$	[25]
Ursa Major II	085130.0+630748	17.50	±0.30	[25]	TRGB	31.6	±4.7	−116.5	±1.9	[25]
HYDRA 1	085536.0+033600	15.52	±0.05	[100]	MS	12.7	±0.3	89	±1.4	[100]
Antlia II	093532.8−364602	20.6	±0.11	[101]	BHB	132	±7	288.8	±0.4	[102]
Segue 1	100703.2+160425	16.8	±0.20	[25]	CMD	22.9	±2.2	208.5	±0.9	[25]
Leo I	100826.9+121829	22.02	±0.13	[25]	TRGB	254	±16	282.5	±0.1	[25]
Sextans dSph	101303.0−013652	19.67	±0.10	[25]	TRGB	85.9	±4.0	224.2	±0.1	[25]
Sextans II	102544.9−003752	20.50	±0.20	[103]	HB	126	±12			
Ursa Major I	103448.8+515606	19.93	±0.10	[25]	TRGB	97	±5	−55.3	±1.4	[25]
Willman 1	104921.0+510260	17.90	±0.40	[25]	CMD	38.0	±7.7	−12.8	±1	[26]
Leo II	111329.2+220917	21.84	±0.13	[25]	TRGB	233	±14	78	±0.1	[25]
Leo V	113109.6+021312	21.46	±0.16	[25]	TRGB	196	±15	170.9	$^{+2.1}_{-1.9}$	[25]
Leo IV	113257.0+003160	20.94	±0.09	[25]	HB	154	±7	132.3	±1.4	[25]
Crater	113615.8−105240	20.81	±0.12	[104]	HB	145	±8	149.3	±1.2	[105]
Crater II	114914.4−182447	20.35	±0.02	[25]	TRGB	118	±1	89.3	±0.3	[102]
Virgo I	120009.6+004048	19.80	±0.20	[25]	HB	91	±9			
Hydra II	122142.1−315907	20.64	±0.16	[25]	TRGB	134	±10	303.1	±1.4	[25]
Coma Berenices	122658.4+235442	18.13	±0.08	[25]	HB	42.3	±1.6	98.1	±0.9	[25]
Centaurus I	123820.4−405407	20.33	±0.10	[106]	HB	116	±6			
Canes Venatici II	125710.0+341915	21.02	±0.06	[25]	HB	160	±5	−129	±1.2	[25]
Canes Venatici I	132803.5+333321	21.69	±0.10	[25]	TRGB	218	±10	30.9	±0.6	[107]
Bootes III	135712.0+264800	18.35	±0.10	[108]	HB	46.8	±2.2	197.5	±3.8	[23]
Bootes II	135808.0+125054	18.10	±0.06	[25]	TRGB	41.7	±1.2	−117	±5.2	[25]
Bootes I	140005.0+143015	19.11	±0.08	[25]	HB	66.4	±2.5	101.8	±0.7	[26]

Table A1. *Cont.*

Name	J2000	$(m-M)_0$			Method	D		V_h		
		mag				kpc		km s^{-1}		
Ursa Minor	150911.3+671252	19.40	±0.10	[25]	TRGB	75.9	±3.6	−246.9	±0.1	[25]
Bootes IV	153445.4+434334	21.60	±0.20	[25]	HB	209	±20			
Draco II	155247.6+643355	16.67	±0.05	[25]	TRGB	21.6	±0.5	342.5	$^{+1.1}_{-1.2}$	[25]
DELVE 1	163054.0+005819	16.39	±0.10	[106]	HB	19.0	±0.9			
Hercules	163103.6+124724	20.84	±0.20	[25]	TRGB	147	±14	46.4	±1.3	[109]
Draco	172001.4+575434	19.40	±0.17	[25]	TRGB	76	±6	−291	±0.1	[25]
Milky Way	174540.0−290028	14.55	±0.01	[110]	Direct	8.1	±0.0	−9.5	±0.0	[34]
Sagittarius dSph	185503.1−302842	17.10	±0.15	[111]	TRGB	26.3	±1.9	140	±2	[112]
Sagittarius II	195240.5−220405	19.32	$^{+0.03}_{-0.02}$	[25]	CMD	73.1	$^{+1.0}_{-0.7}$	−177.2	$^{+0.5}_{-0.6}$	[113]
Indus II	203852.8−460936	21.65	±0.16	[25]	CMD	214	±16			
Indus I	210850.0−510949	20.00	±0.20	[25]	HB	100	±10			
Segue 3	212131.0+190702	16.16	±0.09	[114]	CMD	17.1	±0.7	−167.1	±1.5	[114]
Grus II	220404.8−462624	18.62	±0.21	[25]	CMD	53	±5	−110	±0.5	[25]
Pegasus III	222422.6+052512	21.56	±0.20	[25]	CMD	205	±20	−222.9	±2.6	[25]
Aquarius II	223355.5−091939	20.16	±0.07	[25]	TRGB	108	±4	−71.1	±2.5	[25]
Tucana II	225155.1−583408	18.80	±0.20	[25]	HB	58	±6	−129.1	±3.5	[25]
Grus I	225642.4−500948	20.40	±0.20	[25]	TRGB	120	±12	−140.5	$^{+2.4}_{-1.6}$	[25]
Pisces II	225831.0+055709	21.31	±0.17	[25]	TRGB	183	±15	−226.5	±2.7	[25]
Tucana V	233724.0−631612	18.71	±0.34	[25]	CMD	55	±9	−36.2	$^{+2.5}_{-2.2}$	[25]
Phoenix II	233959.4−542422	19.60	±0.15	[25]	HB	83	±6	32.4	$^{+3.7}_{-3.8}$	[115]
Tucana III	235636.0−593600	17.01	±0.16	[25]	TRGB	25.2	±1.9	−102.3	±0.4	[26]

Notes. The columns contain (1) galaxy name; (2) J2000 equatorial coordinates; (3–5) distance modulus, $(m-M)_0$, and its source; (6) distance determination method: Blue Horizontal Branch (BHB), Cepheids (Cep), Color-Magnitude Diagram (CMD), the S2 orbit around the supermassive black hole in our Galaxy (Direct), Horizontal Branch (HB), Main Sequence (MS), Tip of the Red Giant Branch (TRGB); (7–8) heliocentric distance, D, in kpc; (9–11) heliocentric line-of-sight velocity, V_h, in km s^{-1}, and its source.

Appendix B. List of Satellites of the Andromeda Galaxy

Table A2. Known satellites of the Andromeda Galaxy.

Name	Alt Name	J2000	$(m-M)_0$			Method	D		V_h		
			mag				kpc		km s^{-1}		
PAndAS-05		000024.1+435535							−183.0	±7.0	[116]
And XVIII		000214.5+450520	25.43	$^{+0.05}_{-0.03}$	[117]	HB	1219	$^{+28}_{-17}$	−332.1	±2.7	[118]
PAndAS-04		000442.9+472142							−397.0	±7.0	[116]
And XX		000730.7+350756	24.35	±0.08	[27]	RR Lyr	741	±28	−456.2	$^{+3.0}_{-3.4}$	[118]
IC 10		002024.5+591730	24.50	±0.12	[119]	TRGB	794	±45	−348.0	±2.9	[120]
And XXVI		002345.6+475558	24.48	$^{+0.06}_{-0.07}$	[27]	RR Lyr	787	$^{+22}_{-26}$	−260.6	$^{+4.0}_{-3.7}$	[118]
And XXV		003008.9+465107	24.38	$^{+0.07}_{-0.06}$	[27]	RR Lyr	752	$^{+25}_{-21}$	−107.8	$^{+1.0}_{-0.9}$	[118]
NGC 147		003350.8+483028	24.33	±0.06	[27]	RR Lyr	735	±21	−193.0	±3.0	[118]
And III		003533.8+362952	24.29	±0.05	[27]	RR Lyr	721	±17	−344.3	±1.7	[118]
Cas III	And XXXII	003559.4+513335	24.52	±0.06	[27]	RR Lyr	802	±22	−371.6	±0.7	[121]
And XXX		003634.9+493848	23.74	±0.06	[27]	RR Lyr	560	±16	−141.4	$^{+5.8}_{-6.7}$	[118]
And XVII		003707.0+441920	24.40	±0.07	[27]	RR Lyr	759	±25	−251.1	$^{+1.5}_{-1.6}$	[118]
And XXVII		003727.1+452313	24.59	±0.12	[122]	HB	828	±47	−534.8	$^{+5.4}_{-4.9}$	[118]
NGC 185		003858.0+482010	24.06	±0.06	[27]	RR Lyr	649	±18	−202.0	±3.0	[118]
NGC 205		004022.5+414111	24.61	±0.06	[27]	RR Lyr	836	±23	−241.0	±3.0	[118]
M 32		004242.1+405259	24.44	±0.06	[27]	RR Lyr	773	±22	−200.0	±6.0	[118]
M 31		004244.5+411609	24.45	±0.06	[27]	RR Lyr	776	±22	−301.0	±1.0	[118]
And I		004540.0+380214	24.45	±0.05	[27]	RR Lyr	776	±18	−376.3	±2.2	[118]
And XI		004620.0+334805	24.38	±0.07	[27]	RR Lyr	752	±25	−427.0	$^{+2.9}_{-2.8}$	[118]
And XII		004727.0+342229	24.28	$^{+0.08}_{-0.07}$	[27]	RR Lyr	718	$^{+27}_{-24}$	−557.1	±1.7	[118]
Bol 520		005042.4+325559	24.00	±0.20	[123]	TRGB	631	±61	−370.0	±5.0	[124]
And XIV		005135.0+294149	24.44	±0.06	[27]	RR Lyr	773	±22	−480.6	±1.2	[118]
And XIII		005151.0+330016	24.57	±0.07	[27]	RR Lyr	820	±27	−185.4	±2.4	[118]
And IX		005252.8+431200	24.60	±0.06	[27]	RR Lyr	832	±23	−209.4	±2.5	[118]
PAndAS-48		005928.2+312910	24.57	±0.11	[125]	HB	820	±43	−250.0	±5.0	[116]
And XVI		005929.8+322236	23.57	±0.08	[27]	RR Lyr	518	±19	−367.3	±2.8	[118]

Table A2. *Cont.*

Name	Alt Name	J2000	$(m-M)_0$			Method	D		V_h		
			mag				kpc		km s^{-1}		
PAndAS-50		010150.6+481819							−323.0	±7.0	[116]
LGS 3	Pisces I	010355.0+215306	23.91	±0.05	[27]	RR Lyr	605	±14	−286.5	±0.3	[118]
And X		010633.7+444816	24.00	±0.06	[27]	RR Lyr	631	±18	−164.1	±1.7	[118]
And V		011017.1+473741	24.58	±0.06	[27]	RR Lyr	824	±23	−397.4	±1.5	[118]
And XV		011418.7+380703	24.37	±0.05	[27]	RR Lyr	748	±17	−323.0	±1.4	[118]
And II		011629.8+332509	24.12	±0.05	[27]	RR Lyr	667	$^{+16}_{-16}$	−193.6	±1.0	[118]
And XXIV		011830.0+462258	23.92	±0.07	[27]	RR Lyr	608	±20	−127.8	$^{+5.3}_{-5.4}$	[118]
And XXIX		011830.0+304520	24.26	±0.06	[27]	RR Lyr	711	±20	−194.4	±1.5	[126]
Tri III	Pisces VII	012141.3+262332	24.81	$^{+0.15}_{-0.13}$	[125]	TRGB	916	$^{+65}_{-53}$	−138.6	±0.5	[127]
PAndAS-56		012303.5+415511							−239.0	±8.0	[116]
And XXII		012740.0+280525	24.39	±0.07	[27]	RR Lyr	755	±25	−129.0	$^{+2.1}_{-2.2}$	[118]
PAndAS-57		012747.5+404047							−186.0	±6.0	[116]
PAndAS-58		012902.1+404708							−167.0	±10.0	[116]
And XXIII		012921.8+384308	24.36	±0.07	[27]	RR Lyr	745	±24	−242.7	±1.0	[118]
M 33		013350.8+303937	24.67	±0.06	[27]	RR Lyr	859	±24	−180.0	±1.0	[118]
Per I	And XXXIII	030123.6+405918	24.24	±0.06	[27]	RR Lyr	705	±20	−325.9	±3.0	[121]
And XXVIII		223241.2+311358	24.36	±0.05	[27]	RR Lyr	745	±17	−326.2	±2.7	[126]
Lac I	And XXXI	225816.3+411728	24.36	±0.05	[27]	RR Lyr	745	±17	−198.4	±1.1	[121]
Cas dSph	And VII	232631.8+504032	24.40	±0.06	[27]	RR Lyr	759	±21	−307.2	±1.3	[118]
Pegasus	Peg DIG	232827.6+144434	24.74	±0.05	[27]	RR Lyr	887	±21	−184.5	±0.3	[118]
Peg dSph	And VI	235146.9+243557	24.23	±0.06	[27]	RR Lyr	702	±20	−340.8	±1.9	[118]
And XXI		235447.7+422815	24.44	$^{+0.06}_{-0.07}$	[27]	RR Lyr	773	$^{+22}_{-25}$	−362.7	±0.8	[118]
PAndAS-01		235712.0+433308							−333.0	±21.0	[116]
PAndAS-02		235755.6+414649							−226.0	±4.0	[116]
And XIX		235855.6+350237	24.55	$^{+0.09}_{-0.08}$	[27]	RR Lyr	813	$^{+34}_{-31}$	−111.2	$^{+1.2}_{-1.3}$	[118]

Notes. The columns contain (1) galaxy name; (2) alternative name; (3) J2000 equatorial coordinates; (4–6) distance modulus, $(m-M)_0$, and its source; (7) distance measurement method: Horizontal Branch (HB), RR Lyrae variables (RR Lyr), Tip of the Red Giant Branch (TRGB); (8–9) heliocentric distance, D, in kpc; (10–12) heliocentric line-of-sight velocity, V_h, in km/s, and its source.

Appendix C. List of the Milky Way Mass Estimates

Table A3 presents a compilation of estimates of the virial mass of our Galaxy within its virial radius of 200 kpc, based on publications over the past 15 years, starting from 2010. The columns provide the following information: (1) a reference to the authors, as presented in Figure 5; (2) the mass of the Galaxy, M_{vir}, within the virial radius of 200 kpc; (3) a maximum radius, R_{max}, probed by the mass tracers; (4) a citation to the corresponding article. Only studies that analyze the satellite motion can directly measure the mass within the virial radius. In all other cases, the virial mass within ∼200 kpc is estimated using a model of the gravitational potential of our Galaxy. Below is a brief description of the methods presented in the table.

Escape Velocities. This method analyzes the tail of the velocity distribution of the halo stars (so-called high-velocity stars) to estimate the escape speed $v_{esc}(r) = \sqrt{2|\Phi(r)|}$ from the Galaxy.

Rotation curve method bases on the measurement of the circular velocities of stars and gas. Inner regions use HI/CO gas kinematics, while outer regions rely on tracers like red giants and masers, combined with Gaia proper motions.

Stellar streams. Tidal streams, such as GD-1 and Sagittarius, are sensitive probes of the Galactic potential. Orbit-fitting and N-body simulations model their dynamics constraining mass at intermediate radii 20–100 kpc. Challenges include separating the host potential's effects from subhalo perturbations.

Spherical Jeans Equation connects the radial velocity dispersion, σ_r, the radial density density profile, ρ_*, and the velocity anisotropy, β, of the mass tracers with the underlying gravitational potential. It assumes that a system is a spherically symmetric and in a steady-state.

Distribution Function approach models the gravitational potential by reconstructing the phase–space distribution of tracers (halo stars, globular clusters) using integrals of motion or action.

Kinematics of Satellites. The motions of satellite galaxies and globular clusters probe the outer halo mass. Methods include timing arguments (for bound systems like Leo I) and tracer mass estimators, often compared with cosmological simulations.

Table A3. Milky Way virial mass obtained by different methods since 2010.

Authors	M_{vir} $\times 10^{11}$ $M_\odot$		R_{max} kpc	Ref.
Escape Velocities				
Prudil et al. (2022)	8.3	$^{+2.9}_{-1.6}$	20	[42]
Roche et al. (2024)	6.4	$^{+1.5}_{-1.4}$	11	[43]
Rotation Curve				
McMillan (2011)	12.6	± 2.4	8	[44]
Bovy et al. (2012)	~ 8.0		14	[45]
Huang et al. (2016)	8.5	$^{+0.7}_{-0.8}$	25	[46]
Eilers et al. (2019)	7.25	± 0.26	25	[47]
Cautun et al. (2020)	10.8	$^{+2.0}_{-1.4}$	20	[48]
Ablimit et al. (2020)	8.22	± 0.52	19	[49]
Zhou et al. (2023)	8.05	± 1.15	30	[6]
Sylos Labini et al. (2023)	6.5	± 0.3	28	[50]
Klačka et al. (2024)	13.4	± 0.1	25	[51]
Streams				
Craig et al. (2022)	15.0	± 3.2		[52]
Spherical Jeans Equation				
Gnedin et al. (2010)	16.0	± 3.0	80	[53]
Kafle et al. (2012)	9.0	$^{+4.0}_{-3.0}$	60	[54]
Kafle et al. (2014)	8.0	$^{+3.1}_{-1.6}$	160	[55]
Zhai et al. (2018)	10.8	$^{+1.7}_{-1.4}$	120	[56]
Bird et al. (2022)	$[5.5^{+1.5}_{-1.1}$–$10.0^{+6.7}_{-3.3}]$		70	[57]
Distribution Function				
Eadie et al. (2015)	13.7	$^{+1.4}_{-1.0}$	261	[58]
Eadie and Harris (2016)	9.02	$^{+1.7}_{-3.3}$	200	[59]
Sohn et al. (2018)	20.5	$^{+9.7}_{-7.9}$	100	[60]
Watkins et al. (2019)	15.4	$^{+7.5}_{-4.4}$	40	[61]
Vasiliev (2019)	12	$^{+15}_{-5}$	50	[8]
Posti and Helmi (2019)	13	± 3	20	[62]
Li et al. (2020)	12.3	$^{+2.1}_{-1.8}$	200	[63]
Deason et al. (2021)	10.1	± 2.4	100	[64]
Shen et al. (2022)	10.8	$^{+1.2}_{-1.1}$	145	[65]
Kinematics of Satellites				
Watkins et al. (2010)	14.0	± 3.0	300	[3]
Busha et al. (2011)	12.0	$^{+7.0}_{-4.0}$	300	[66]
González et al. (2013)	11.5	$^{+4.8}_{-3.4}$	200	[67]
Boylan-Kolchin et al. (2013)	16	$^{+8}_{-6}$	261	[38]

Table A3. *Cont.*

Authors	M_{vir} $\times 10^{11}\ M_\odot$		R_{max} kpc	**Ref.**
Cautun et al. (2014)	7.8	$^{+5.7}_{-3.3}$	200	[68]
Barber et al. (2014)	11.0	$^{+4.5}_{-2.9}$	200	[69]
Patel et al. (2017)	8.3	$^{+7.7}_{-5.5}$	200	[70]
Patel et al. (2018)	6.8	$^{+2.3}_{-2.6}$	200	[71]
Fritz et al. (2020)	15.1	$^{+4.5}_{-4.0}$	300	[72]
Rodriguez Wimberly et al. (2022)	$\sim$ 10–12		300	[73]
Kravtsov and Winney (2024)	9.96	± 1.45	200	[9]
this work	7.9	± 2.3	236	

Appendix D. List of the M 31 Mass Estimates

Table A4 contains a compilation from the literature of recent measurements (from the 2010) of the virial mass of the Andromeda Galaxy. It contains the following information: (1) a reference to the authors, as presented in Figure 8; (2) the M 31 mass within the virial radius of 200–300 kpc; (3) a maximal radius, R_{max}, probed by the mass tracers; (4) a citation to the corresponding article. A brief description of the methods listed in the table is provided below.

Table A4. M 31 virial mass estimates obtained by different methods since 2010.

Authors	M_{vir} $\times 10^{11}\ M_\odot$		R_{max} kpc	**Ref.**
Rotation Curve				
Tamm et al. (2012)	9.5	± 1.5	25	[81]
Hayashi and Chiba (2014)	18.2	$^{+4.9}_{-3.9}$	30	[82]
Sofue (2015)	13.7	± 5.2	31	[83]
Zhang et al. (2024)	11.4	$^{+5.1}_{-3.5}$	125	[84]
Substructure				
Fardal et al. (2013)	19.9	$^{+5.2}_{-4.1}$		[85]
Globular Clusters				
Veljanoski et al. (2013)	13.5	± 3.5	130	[86]
Kinematics of Satellites				
Watkins et al. (2010)	14	± 4	300	[3]
Patel et al. (2017)	13.7	$^{+13.9}_{-7.5}$	300	[87]
Patel and Mandel (2023)	30.2	$^{+13.0}_{-6.9}$	300	[76]
this work	15.5	± 3.4	292	
Local Group Kinematics				
van der Marel et al. (2012)	15.4	± 3.9		[88]
Diaz et al. (2014)	17	± 3		[89]
Peñarrubia et al. (2014)	15	± 3		[22]
Peñarrubia et al. (2016)	13.3	$^{+3.9}_{-3.3}$		[90]

Rotation Curve measures circular velocities of tracers (stars, gas) to determine the mass distribution. In the case of M 31, HI observations extend to 40 kpc, revealing flat rotation curves that indicate dark matter dominance. The virial mass within $\sim$200 kpc is based on a model of the M 31 gravitational potential.

Subsctructure Tidal streams (e.g., the Giant Stream) constrain halo mass and shape using N-body simulations. Progenitor properties and merger history must be taken into accounted.

Globular Clusters (GC) trace mass at intermediate radii of 20–200 kpc. The advantage is the large number of known GC. However, a major challenge lies in distinguishing between in situ and recently accreted clusters, as well as accounting for the tidal effects.

Kinematics of Satellites uses the velocities and distances of the dwarf satellites to infer gravitational mass at 100–300 kpc. Challenges include small sample sizes (<30 satellites) and potential disequilibrium due to ongoing mergers.

Local Group Kinematics The M 31-MW motion provides a total mass estimate using the timing argument. Modern approaches include proper motions and perturbations from the LMC, but depend on the assumed mass ratios.

Notes

[1] The energy, E_0, and the angular momentum, J_0, define the orbit of a satellite within a spherically symmetric potential, while the delta functions represent the phase–space distribution under the condition that the energy and angular momentum are constrained to these specific values.

[2] Tri III has already been excluded in the previous step due to insufficient distance measurement accuracy.

[3] http://leda.univ-lyon1.fr (accessed on 26 April 2025).

References

1. Bahcall, J.N.; Tremaine, S. Methods for determining the masses of spherical systems. I. Test particles around a point mass. *Astrophys. J.* **1981**, *244*, 805–819. [CrossRef]
2. Heisler, J.; Tremaine, S.; Bahcall, J.N. Estimating the masses of galaxy groups: Alternatives to the virial theorem. *Astrophys. J.* **1985**, *298*, 8–17. [CrossRef]
3. Watkins, L.L.; Evans, N.W.; An, J.H. The masses of the Milky Way and Andromeda galaxies. *Mon. Not. R. Astron. Soc.* **2010**, *406*, 264–278.
4. Anand, G.S.; Rizzi, L.; Tully, R.B.; Shaya, E.J.; Karachentsev, I.D.; Makarov, D.I.; Makarova, L.; Wu, P.F.; Dolphin, A.E.; Kourkchi, E. The Extragalactic Distance Database: The Color-Magnitude Diagrams/Tip of the Red Giant Branch Distance Catalog. *Astron. J.* **2021**, *162*, 80.
5. Tully, R.B.; Rizzi, L.; Shaya, E.J.; Courtois, H.M.; Makarov, D.I.; Jacobs, B.A. The Extragalactic Distance Database. *Astron. J.* **2009**, *138*, 323–331. [CrossRef]
6. Zhou, Y.; Li, X.; Huang, Y.; Zhang, H. The Circular Velocity Curve of the Milky Way from 5 to 25 kpc Using Luminous Red Giant Branch Stars. *Astrophys. J.* **2023**, *946*, 73.
7. Navarro, J.F.; Frenk, C.S.; White, S.D.M. The assembly of galaxies in a hierarchically clustering universe. *Mon. Not. R. Astron. Soc.* **1995**, *275*, 56–66.
8. Vasiliev, E. Proper motions and dynamics of the Milky Way globular cluster system from Gaia DR2. *Mon. Not. R. Astron. Soc.* **2019**, *484*, 2832–2850.
9. Kravtsov, A.; Winney, S. Effect of the Large Magellanic Cloud on the kinematics of Milky Way satellites and virial mass estimate. *Open J. Astrophys.* **2024**, *7*, 50.
10. Karachentsev, I.D.; Kashibadze, O.G.; Makarov, D.I.; Tully, R.B. The Hubble flow around the Local Group. *Mon. Not. R. Astron. Soc.* **2009**, *393*, 1265–1274.
11. Libeskind, N.I.; Carlesi, E.; Grand, R.J.J.; Khalatyan, A.; Knebe, A.; Pakmor, R.; Pilipenko, S.; Pawlowski, M.S.; Sparre, M.; Tempel, E.; et al. The HESTIA project: Simulations of the Local Group. *Mon. Not. R. Astron. Soc.* **2020**, *498*, 2968–2983.
12. Weinberger, R.; Springel, V.; Pakmor, R. The AREPO Public Code Release. *Astrophys. J.* **2020**, *248*, 32.
13. Tully, R.B.; Courtois, H.M.; Dolphin, A.E.; Fisher, J.R.; Héraudeau, P.; Jacobs, B.A.; Karachentsev, I.D.; Makarov, D.; Makarova, L.; Mitronova, S.; et al. Cosmicflows-2: The Data. *Astron. J.* **2013**, *146*, 86.
14. Doumler, T.; Hoffman, Y.; Courtois, H.; Gottlöber, S. Reconstructing cosmological initial conditions from galaxy peculiar velocities—I. Reverse Zeldovich Approximation. *Mon. Not. R. Astron. Soc.* **2013**, *430*, 888–901.
15. Grand, R.J.J.; Gómez, F.A.; Marinacci, F.; Pakmor, R.; Springel, V.; Campbell, D.J.R.; Frenk, C.S.; Jenkins, A.; White, S.D.M. The Auriga Project: The properties and formation mechanisms of disc galaxies across cosmic time. *Mon. Not. R. Astron. Soc.* **2017**, *467*, 179–207.
16. McCall, M.L. A Council of Giants. *Mon. Not. R. Astron. Soc.* **2014**, *440*, 405–426.
17. Smith, S.E.T.; Cerny, W.; Hayes, C.R.; Sestito, F.; Jensen, J.; McConnachie, A.W.; Geha, M.; Navarro, J.F.; Li, T.S.; Cuillandre, J.C.; et al. The Discovery of the Faintest Known Milky Way Satellite Using UNIONS. *Astrophys. J.* **2024**, *961*, 92.

18. Wang, W.; Han, J.; Cautun, M.; Li, Z.; Ishigaki, M.N. The mass of our Milky Way. *Sci. China Phys. Mech. Astron.* **2020**, *63*, 109801.
19. Bobylev, V.V.; Baykova, A.T. Modern Estimates of the Mass of the Milky Way. *Astron. Rep.* **2023**, *67*, 812–823. [CrossRef]
20. Bhattacharya, S. Weighing Andromeda: Mass estimates of the M∼31 galaxy. *arXiv* **2023**, arXiv:2305.03293.
21. Carlesi, E.; Hoffman, Y.; Libeskind, N.I. Estimation of the masses in the local group by gradient boosted decision trees. *Mon. Not. R. Astron. Soc.* **2022**, *513*, 2385–2393.
22. Peñarrubia, J.; Ma, Y.Z.; Walker, M.G.; McConnachie, A. A dynamical model of the local cosmic expansion. *Mon. Not. R. Astron. Soc.* **2014**, *443*, 2204–2222.
23. Kaisina, E.I.; Makarov, D.I.; Karachentsev, I.D.; Kaisin, S.S. Observational database for studies of nearby universe. *Astrophys. Bull.* **2012**, *67*, 115–122. [CrossRef]
24. Kashibadze, O.G.; Karachentsev, I.D. Cosmic flow around local massive galaxies. *Astron. Astrophys.* **2018**, *609*, A11.
25. McConnachie, A.W.; Venn, K.A. Revised and New Proper Motions for Confirmed and Candidate Milky Way Dwarf Galaxies. *Astron. J.* **2020**, *160*, 124.
26. Pace, A.B.; Erkal, D.; Li, T.S. Proper Motions, Orbits, and Tidal Influences of Milky Way Dwarf Spheroidal Galaxies. *Astrophys. J.* **2022**, *940*, 136.
27. Savino, A.; Weisz, D.R.; Skillman, E.D.; Dolphin, A.; Kallivayalil, N.; Wetzel, A.; Anderson, J.; Besla, G.; Boylan-Kolchin, M.; Bullock, J.S.; et al. The Hubble Space Telescope Survey of M31 Satellite Galaxies. I. RR Lyrae-based Distances and Refined 3D Geometric Structure. *Astrophys. J.* **2022**, *938*, 101.
28. Drlica-Wagner, A.; Bechtol, K.; Mau, S.; McNanna, M.; Nadler, E.O.; Pace, A.B.; Li, T.S.; Pieres, A.; Rozo, E.; Simon, J.D.; et al. Milky Way Satellite Census. I. The Observational Selection Function for Milky Way Satellites in DES Y3 and Pan-STARRS DR1. *Astrophys. J.* **2020**, *893*, 47.
29. Makarov, D.; Prugniel, P.; Terekhova, N.; Courtois, H.; Vauglin, I. HyperLEDA. III. The catalogue of extragalactic distances. *Astron. Astrophys.* **2014**, *570*, A13.
30. Pawlowski, M.S. Phase-Space Correlations among Systems of Satellite Galaxies. *Galaxies* **2021**, *9*, 66.
31. Conn, A.R.; Lewis, G.F.; Ibata, R.A.; Parker, Q.A.; Zucker, D.B.; McConnachie, A.W.; Martin, N.F.; Valls-Gabaud, D.; Tanvir, N.; Irwin, M.J.; et al. The Three-dimensional Structure of the M31 Satellite System; Strong Evidence for an Inhomogeneous Distribution of Satellites. *Astrophys. J.* **2013**, *766*, 120.
32. Gaia Collaboration; Brown, A.G.A.; Vallenari, A.; Prusti, T.; de Bruijne, J.H.J.; Babusiaux, C.; Bailer-Jones, C.A.L.; Biermann, M.; Evans, D.W.; Eyer, L.; et al. Gaia Data Release 2. Summary of the contents and survey properties. *Astron. Astrophys.* **2018**, *616*, A1.
33. Makarov, D.; Khoperskov, S.; Makarov, D.; Makarova, L.; Libeskind, N.; Salomon, J.B. The LMC impact on the kinematics of the Milky Way satellites: Clues from the running solar apex. *Mon. Not. R. Astron. Soc.* **2023**, *521*, 3540–3552.
34. Akhmetov, V.S.; Bucciarelli, B.; Crosta, M.; Lattanzi, M.G.; Spagna, A.; Re Fiorentin, P.; Bannikova, E.Y. A new kinematic model of the Galaxy: Analysis of the stellar velocity field from Gaia Data Release 3. *Mon. Not. R. Astron. Soc.* **2024**, *530*, 710–729.
35. Reid, M.J.; Brunthaler, A. The Proper Motion of Sagittarius A*. III. The Case for a Supermassive Black Hole. *Astrophys. J.* **2020**, *892*, 39.
36. GRAVITY Collaboration; Abuter, R.; Amorim, A.; Bauböck, M.; Berger, J.P.; Bonnet, H.; Brandner, W.; Clénet, Y.; Davies, R.; de Zeeuw, P.T.; et al. Improved GRAVITY astrometric accuracy from modeling optical aberrations. *Astron. Astrophys.* **2021**, *647*, A59.
37. Bajkova, A.T.; Bobylev, V.V. Galactic orbits of selected companions of the Milky Way. *Astron. Rep.* **2017**, *61*, 727–738.
38. Boylan-Kolchin, M.; Bullock, J.S.; Sohn, S.T.; Besla, G.; van der Marel, R.P. The Space Motion of Leo I: The Mass of the Milky Way's Dark Matter Halo. *Astrophys. J.* **2013**, *768*, 140.
39. Pacucci, F.; Ni, Y.; Loeb, A. Extreme Tidal Stripping May Explain the Overmassive Black Hole in Leo I: A Proof of Concept. *Astrophys. J.* **2023**, *956*, L37.
40. Bland-Hawthorn, J.; Gerhard, O. The Galaxy in Context: Structural, Kinematic, and Integrated Properties. *Annu. Rev. Astron. Astrophys.* **2016**, *54*, 529–596.
41. Hunt, J.A.S.; Vasiliev, E. Milky Way dynamics in light of Gaia. *New Astron. Rev.* **2025**, *100*, 101721.
42. Prudil, Z.; Koch-Hansen, A.J.; Lemasle, B.; Grebel, E.K.; Marchetti, T.; Hansen, C.J.; Crestani, J.; Braga, V.F.; Bono, G.; Chaboyer, B.; et al. Milky Way archaeology using RR Lyrae and type II Cepheids. II. High-velocity RR Lyrae stars and Milky Way mass. *Astron. Astrophys.* **2022**, *664*, A148.
43. Roche, C.; Necib, L.; Lin, T.; Ou, X.; Nguyen, T. The Escape Velocity Profile of the Milky Way from Gaia DR3. *Astrophys. J.* **2024**, *972*, 70.
44. McMillan, P.J. Mass models of the Milky Way. *Mon. Not. R. Astron. Soc.* **2011**, *414*, 2446–2457.
45. Bovy, J.; Allende Prieto, C.; Beers, T.C.; Bizyaev, D.; da Costa, L.N.; Cunha, K.; Ebelke, G.L.; Eisenstein, D.J.; Frinchaboy, P.M.; García Pérez, A.E.; et al. The Milky Way's Circular-velocity Curve between 4 and 14 kpc from APOGEE data. *Astrophys. J.* **2012**, *759*, 131.

46. Huang, Y.; Liu, X.W.; Yuan, H.B.; Xiang, M.S.; Zhang, H.W.; Chen, B.Q.; Ren, J.J.; Wang, C.; Zhang, Y.; Hou, Y.H.; et al. The Milky Way's rotation curve out to 100 kpc and its constraint on the Galactic mass distribution. *Mon. Not. R. Astron. Soc.* **2016**, *463*, 2623–2639.
47. Eilers, A.C.; Hogg, D.W.; Rix, H.W.; Ness, M.K. The Circular Velocity Curve of the Milky Way from 5 to 25 kpc. *Astrophys. J.* **2019**, *871*, 120.
48. Cautun, M.; Benítez-Llambay, A.; Deason, A.J.; Frenk, C.S.; Fattahi, A.; Gómez, F.A.; Grand, R.J.J.; Oman, K.A.; Navarro, J.F.; Simpson, C.M. The milky way total mass profile as inferred from Gaia DR2. *Mon. Not. R. Astron. Soc.* **2020**, *494*, 4291–4313.
49. Ablimit, I.; Zhao, G.; Flynn, C.; Bird, S.A. The Rotation Curve, Mass Distribution, and Dark Matter Content of the Milky Way from Classical Cepheids. *Astrophys. J.* **2020**, *895*, L12.
50. Sylos Labini, F.; Chrobáková, Ž.; Capuzzo-Dolcetta, R.; López-Corredoira, M. Mass Models of the Milky Way and Estimation of Its Mass from the Gaia DR3 Data Set. *Astrophys. J.* **2023**, *945*, 3.
51. Klačka, J.; Šturc, M.; Puha, E. Milky Way: New Galactic mass model for orbit computations. *arXiv* **2024**, arXiv:2407.12551.
52. Craig, P.A.; Chakrabarti, S.; Baum, S.; Lewis, B.T. An estimate of the mass of the Milky Way from the Magellanic Stream. *Mon. Not. R. Astron. Soc.* **2022**, *517*, 1737–1749. [CrossRef]
53. Gnedin, O.Y.; Brown, W.R.; Geller, M.J.; Kenyon, S.J. The Mass Profile of the Galaxy to 80 kpc. *Astrophys. J.* **2010**, *720*, L108–L112.
54. Kafle, P.R.; Sharma, S.; Lewis, G.F.; Bland-Hawthorn, J. Kinematics of the Stellar Halo and the Mass Distribution of the Milky Way Using Blue Horizontal Branch Stars. *Astrophys. J.* **2012**, *761*, 98.
55. Kafle, P.R.; Sharma, S.; Lewis, G.F.; Bland-Hawthorn, J. On the Shoulders of Giants: Properties of the Stellar Halo and the Milky Way Mass Distribution. *Astrophys. J.* **2014**, *794*, 59.
56. Zhai, M.; Xue, X.X.; Zhang, L.; Li, C.D.; Zhao, G.; Yang, C.Q. The mass of the Galactic dark matter halo from ∼9000 LAMOST DR5 K giants. *Res. Astron. Astrophys.* **2018**, *18*, 113. [CrossRef]
57. Bird, S.A.; Xue, X.X.; Liu, C.; Flynn, C.; Shen, J.; Wang, J.; Yang, C.; Zhai, M.; Zhu, L.; Zhao, G.; et al. Milky Way mass with K giants and BHB stars using LAMOST, SDSS/SEGUE, and Gaia: 3D spherical Jeans equation and tracer mass estimator. *Mon. Not. R. Astron. Soc.* **2022**, *516*, 731–748.
58. Eadie, G.M.; Harris, W.E.; Widrow, L.M. Estimating the Galactic Mass Profile in the Presence of Incomplete Data. *Astrophys. J.* **2015**, *806*, 54.
59. Eadie, G.M.; Harris, W.E. Bayesian Mass Estimates of the Milky Way: The Dark and Light Sides of Parameter Assumptions. *Astrophys. J.* **2016**, *829*, 108.
60. Sohn, S.T.; Watkins, L.L.; Fardal, M.A.; van der Marel, R.P.; Deason, A.J.; Besla, G.; Bellini, A. Absolute Hubble Space Telescope Proper Motion (HSTPROMO) of Distant Milky Way Globular Clusters: Galactocentric Space Velocities and the Milky Way Mass. *Astrophys. J.* **2018**, *862*, 52.
61. Watkins, L.L.; van der Marel, R.P.; Sohn, S.T.; Evans, N.W. Evidence for an Intermediate-mass Milky Way from Gaia DR2 Halo Globular Cluster Motions. *Astrophys. J.* **2019**, *873*, 118.
62. Posti, L.; Helmi, A. Mass and shape of the Milky Way's dark matter halo with globular clusters from Gaia and Hubble. *Astron. Astrophys.* **2019**, *621*, A56.
63. Li, Z.Z.; Qian, Y.Z.; Han, J.; Li, T.S.; Wang, W.; Jing, Y.P. Constraining the Milky Way Mass Profile with Phase-space Distribution of Satellite Galaxies. *Astrophys. J.* **2020**, *894*, 10.
64. Deason, A.J.; Erkal, D.; Belokurov, V.; Fattahi, A.; Gómez, F.A.; Grand, R.J.J.; Pakmor, R.; Xue, X.X.; Liu, C.; Yang, C.; et al. The mass of the Milky Way out to 100 kpc using halo stars. *Mon. Not. R. Astron. Soc.* **2021**, *501*, 5964–5972.
65. Shen, J.; Eadie, G.M.; Murray, N.; Zaritsky, D.; Speagle, J.S.; Ting, Y.S.; Conroy, C.; Cargile, P.A.; Johnson, B.D.; Naidu, R.P.; et al. The Mass of the Milky Way from the H3 Survey. *Astrophys. J.* **2022**, *925*, 1.
66. Busha, M.T.; Marshall, P.J.; Wechsler, R.H.; Klypin, A.; Primack, J. The Mass Distribution and Assembly of the Milky Way from the Properties of the Magellanic Clouds. *Astrophys. J.* **2011**, *743*, 40.
67. González, R.E.; Kravtsov, A.V.; Gnedin, N.Y. Satellites in Milky-Way-like Hosts: Environment Dependence and Close Pairs. *Astrophys. J.* **2013**, *770*, 96.
68. Cautun, M.; Frenk, C.S.; van de Weygaert, R.; Hellwing, W.A.; Jones, B.J.T. Milky Way mass constraints from the Galactic satellite gap. *Mon. Not. R. Astron. Soc.* **2014**, *445*, 2049–2060.
69. Barber, C.; Starkenburg, E.; Navarro, J.F.; McConnachie, A.W.; Fattahi, A. The orbital ellipticity of satellite galaxies and the mass of the Milky Way. *Mon. Not. R. Astron. Soc.* **2014**, *437*, 959–967.
70. Patel, E.; Besla, G.; Sohn, S.T. Orbits of massive satellite galaxies—I. A close look at the Large Magellanic Cloud and a new orbital history for M33. *Mon. Not. R. Astron. Soc.* **2017**, *464*, 3825–3849.
71. Patel, E.; Besla, G.; Mandel, K.; Sohn, S.T. Estimating the Mass of the Milky Way Using the Ensemble of Classical Satellite Galaxies. *Astrophys. J.* **2018**, *857*, 78.
72. Fritz, T.K.; Di Cintio, A.; Battaglia, G.; Brook, C.; Taibi, S. The mass of our Galaxy from satellite proper motions in the Gaia era. *Mon. Not. R. Astron. Soc.* **2020**, *494*, 5178–5193.

73. Rodriguez Wimberly, M.K.; Cooper, M.C.; Baxter, D.C.; Boylan-Kolchin, M.; Bullock, J.S.; Fillingham, S.P.; Ji, A.P.; Sales, L.V.; Simon, J.D. Sizing from the smallest scales: The mass of the Milky Way. *Mon. Not. R. Astron. Soc.* **2022**, *513*, 4968–4982.
74. van der Marel, R.P.; Fardal, M.A.; Sohn, S.T.; Patel, E.; Besla, G.; del Pino, A.; Sahlmann, J.; Watkins, L.L. First Gaia Dynamics of the Andromeda System: DR2 Proper Motions, Orbits, and Rotation of M31 and M33. *Astrophys. J.* **2019**, *872*, 24.
75. Salomon, J.B.; Ibata, R.; Reylé, C.; Famaey, B.; Libeskind, N.I.; McConnachie, A.W.; Hoffman, Y. The proper motion of Andromeda from Gaia EDR3: Confirming a nearly radial orbit. *Mon. Not. R. Astron. Soc.* **2021**, *507*, 2592–2601.
76. Patel, E.; Mandel, K.S. Evidence for a Massive Andromeda Galaxy Using Satellite Galaxy Proper Motions. *Astrophys. J.* **2023**, *948*, 104.
77. Casetti-Dinescu, D.I.; Pawlowski, M.S.; Girard, T.M.; Kanehisa, K.J.; Petroski, A.; Martone, M.; Kozhurina-Platais, V.; Platais, I. HST Proper Motion of Andromeda III. Another Satellite Coorbiting the M31 Satellite Plane. *Astrophys. J.* **2024**, *975*, 138.
78. Collins, M.L.M.; Karim, N.; Martinez-Delgado, D.; Monelli, M.; Tollerud, E.J.; Donatiello, G.; Navabi, M.; Charles, E.; Boschin, W. Pisces VII/Triangulum III—M33's second dwarf satellite galaxy. *Mon. Not. R. Astron. Soc.* **2024**, *528*, 2614–2620.
79. Patel, E.; Carlin, J.L.; Tollerud, E.J.; Collins, M.L.M.; Dooley, G.A. ΛCDM predictions for the satellite population of M33. *Mon. Not. R. Astron. Soc.* **2018**, *480*, 1883–1897.
80. Makarova, L.N.; Makarov, D.I.; Karachentsev, I.D.; Tully, R.B.; Rizzi, L. Star formation history of And XVIII: A dwarf spheroidal galaxy in isolation. *Mon. Not. R. Astron. Soc.* **2017**, *464*, 2281–2289.
81. Tamm, A.; Tempel, E.; Tenjes, P.; Tihhonova, O.; Tuvikene, T. Stellar mass map and dark matter distribution in M 31. *Astron. Astrophys.* **2012**, *546*, A4.
82. Hayashi, K.; Chiba, M. The Prolate Dark Matter Halo of the Andromeda Galaxy. *Astrophys. J.* **2014**, *789*, 62.
83. Sofue, Y. Dark halos of M 31 and the Milky Way. *Publ. Astron. Soc. Jpn.* **2015**, *67*, 75.
84. Zhang, X.; Chen, B.; Chen, P.; Sun, J.; Tian, Z. The rotation curve and mass distribution of M31. *Mon. Not. R. Astron. Soc.* **2024**, *528*, 2653–2666.
85. Fardal, M.A.; Weinberg, M.D.; Babul, A.; Irwin, M.J.; Guhathakurta, P.; Gilbert, K.M.; Ferguson, A.M.N.; Ibata, R.A.; Lewis, G.F.; Tanvir, N.R.; et al. Inferring the Andromeda Galaxy's mass from its giant southern stream with Bayesian simulation sampling. *Mon. Not. R. Astron. Soc.* **2013**, *434*, 2779–2802.
86. Veljanoski, J.; Ferguson, A.M.N.; Mackey, A.D.; Huxor, A.P.; Irwin, M.J.; Côté, P.; Tanvir, N.R.; Bernard, E.J.; Chapman, S.C.; Ibata, R.A.; et al. Kinematics of Outer Halo Globular Clusters in M31. *Astrophys. J.* **2013**, *768*, L33.
87. Patel, E.; Besla, G.; Mandel, K. Orbits of massive satellite galaxies—II. Bayesian estimates of the Milky Way and Andromeda masses using high-precision astrometry and cosmological simulations. *Mon. Not. R. Astron. Soc.* **2017**, *468*, 3428–3449.
88. van der Marel, R.P.; Fardal, M.; Besla, G.; Beaton, R.L.; Sohn, S.T.; Anderson, J.; Brown, T.; Guhathakurta, P. The M31 Velocity Vector. II. Radial Orbit toward the Milky Way and Implied Local Group Mass. *Astrophys. J.* **2012**, *753*, 8.
89. Diaz, J.D.; Koposov, S.E.; Irwin, M.; Belokurov, V.; Evans, N.W. Balancing mass and momentum in the Local Group. *Mon. Not. R. Astron. Soc.* **2014**, *443*, 1688–1703.
90. Peñarrubia, J.; Gómez, F.A.; Besla, G.; Erkal, D.; Ma, Y.Z. A timing constraint on the (total) mass of the Large Magellanic Cloud. *Mon. Not. R. Astron. Soc.* **2016**, *456*, L54–L58.
91. Drlica-Wagner, A.; Bechtol, K.; Rykoff, E.S.; Luque, E.; Queiroz, A.; Mao, Y.Y.; Wechsler, R.H.; Simon, J.D.; Santiago, B.; Yanny, B.; et al. Eight Ultra-faint Galaxy Candidates Discovered in Year Two of the Dark Energy Survey. *Astrophys. J.* **2015**, *813*, 109.
92. Karachentsev, I.D.; Karachentseva, V.E.; Huchtmeier, W.K.; Makarov, D.I. A Catalog of Neighboring Galaxies. *Astron. J.* **2004**, *127*, 2031–2068. [CrossRef]
93. Walker, M.G.; Mateo, M.; Olszewski, E.W.; Sen, B.; Woodroofe, M. Clean Kinematic Samples in Dwarf Spheroidals: An Algorithm for Evaluating Membership and Estimating Distribution Parameters When Contamination is Present. *Astron. J.* **2009**, *137*, 3109–3138.
94. Conn, B.C.; Jerjen, H.; Kim, D.; Schirmer, M. On the Nature of Ultra-faint Dwarf Galaxy Candidates. I. DES1, Eridanus III, and Tucana V. *Astrophys. J.* **2018**, *852*, 68.
95. Cerny, W.; Pace, A.B.; Drlica-Wagner, A.; Ferguson, P.S.; Mau, S.; Adamów, M.; Carlin, J.L.; Choi, Y.; Erkal, D.; Johnson, L.C.; et al. Discovery of an Ultra-faint Stellar System near the Magellanic Clouds with the DECam Local Volume Exploration Survey. *Astrophys. J.* **2021**, *910*, 18.
96. Carlin, J.L.; Sand, D.J.; Muñoz, R.R.; Spekkens, K.; Willman, B.; Crnojević, D.; Forbes, D.A.; Hargis, J.; Kirby, E.; Peter, A.H.G.; et al. Deep Subaru Hyper Suprime-Cam Observations of Milky Way Satellites Columba I and Triangulum II. *Astron. J.* **2017**, *154*, 267.
97. Luque, E.; Pieres, A.; Santiago, B.; Yanny, B.; Vivas, A.K.; Queiroz, A.; Drlica-Wagner, A.; Morganson, E.; Balbinot, E.; Marshall, J.L.; et al. The Dark Energy Survey view of the Sagittarius stream: Discovery of two faint stellar system candidates. *Mon. Not. R. Astron. Soc.* **2017**, *468*, 97–108.

98. Ferrarese, L.; Mould, J.R.; Kennicutt, R.C., Jr.; Huchra, J.; Ford, H.C.; Freedman, W.L.; Stetson, P.B.; Madore, B.F.; Sakai, S.; Gibson, B.K.; et al. The Hubble Space Telescope Key Project on the Extragalactic Distance Scale. XXVI. The Calibration of Population II Secondary Distance Indicators and the Value of the Hubble Constant. *Astrophys. J.* **2000**, *529*, 745–767.
99. Strauss, M.A.; Huchra, J.P.; Davis, M.; Yahil, A.; Fisher, K.B.; Tonry, J. A Redshift Survey of IRAS Galaxies. VII. The Infrared and Redshift Data for the 1.936 Jansky Sample. *Astrophys. J.* **1992**, *83*, 29. [CrossRef]
100. Hargis, J.R.; Kimmig, B.; Willman, B.; Caldwell, N.; Walker, M.G.; Strader, J.; Sand, D.J.; Grillmair, C.J.; Yoon, J.H. Evidence That Hydra I is a Tidally Disrupting Milky Way Dwarf Galaxy. *Astrophys. J.* **2016**, *818*, 39.
101. Torrealba, G.; Belokurov, V.; Koposov, S.E.; Li, T.S.; Walker, M.G.; Sanders, J.L.; Geringer-Sameth, A.; Zucker, D.B.; Kuehn, K.; Evans, N.W.; et al. The hidden giant: Discovery of an enormous Galactic dwarf satellite in Gaia DR2. *Mon. Not. R. Astron. Soc.* **2019**, *488*, 2743–2766.
102. Ji, A.P.; Koposov, S.E.; Li, T.S.; Erkal, D.; Pace, A.B.; Simon, J.D.; Belokurov, V.; Cullinane, L.R.; Da Costa, G.S.; Kuehn, K.; et al. Kinematics of Antlia 2 and Crater 2 from the Southern Stellar Stream Spectroscopic Survey (S^5). *Astrophys. J.* **2021**, *921*, 32.
103. McQuinn, K.B.W.; Mao, Y.Y.; Tollerud, E.J.; Cohen, R.E.; Shih, D.; Buckley, M.R.; Dolphin, A.E. Discovery and Characterization of Two Ultrafaint Dwarfs outside the Halo of the Milky Way: Leo M and Leo K. *Astrophys. J.* **2024**, *967*, 161.
104. Laevens, B.P.M.; Martin, N.F.; Sesar, B.; Bernard, E.J.; Rix, H.W.; Slater, C.T.; Bell, E.F.; Ferguson, A.M.N.; Schlafly, E.F.; Burgett, W.S.; et al. A New Distant Milky Way Globular Cluster in the Pan-STARRS1 3π Survey. *Astrophys. J.* **2014**, *786*, L3.
105. Kirby, E.N.; Simon, J.D.; Cohen, J.G. Spectroscopic Confirmation of the Dwarf Galaxies Hydra II and Pisces II and the Globular Cluster Laevens 1. *Astrophys. J.* **2015**, *810*, 56.
106. Mau, S.; Cerny, W.; Pace, A.B.; Choi, Y.; Drlica-Wagner, A.; Santana-Silva, L.; Riley, A.H.; Erkal, D.; Stringfellow, G.S.; Adamów, M.; et al. Two Ultra-faint Milky Way Stellar Systems Discovered in Early Data from the DECam Local Volume Exploration Survey. *Astrophys. J.* **2020**, *890*, 136.
107. Simon, J.D.; Geha, M. The Kinematics of the Ultra-faint Milky Way Satellites: Solving the Missing Satellite Problem. *Astrophys. J.* **2007**, *670*, 313–331.
108. Grillmair, C.J. Four New Stellar Debris Streams in the Galactic Halo. *Astrophys. J.* **2009**, *693*, 1118–1127.
109. Gregory, A.L.; Collins, M.L.M.; Erkal, D.; Tollerud, E.; Delorme, M.; Hill, L.; Sand, D.J.; Strader, J.; Willman, B. Uncovering the orbit of the hercules dwarf galaxy. *Mon. Not. R. Astron. Soc.* **2020**, *496*, 1092–1104.
110. GRAVITY Collaboration; Abuter, R.; Amorim, A.; Anugu, N.; Bauböck, M.; Benisty, M.; Berger, J.P.; Blind, N.; Bonnet, H.; Brandner, W.; et al. Detection of the gravitational redshift in the orbit of the star S2 near the Galactic centre massive black hole. *Astron. Astrophys.* **2018**, *615*, L15.
111. Monaco, L.; Bellazzini, M.; Ferraro, F.R.; Pancino, E. The distance to the Sagittarius dwarf spheroidal galaxy from the red giant branch tip. *Mon. Not. R. Astron. Soc.* **2004**, *353*, 874–878.
112. Kirby, E.N.; Bullock, J.S.; Boylan-Kolchin, M.; Kaplinghat, M.; Cohen, J.G. The dynamics of isolated Local Group galaxies. *Mon. Not. R. Astron. Soc.* **2014**, *439*, 1015–1027.
113. Longeard, N.; Martin, N.; Ibata, R.A.; Starkenburg, E.; Jablonka, P.; Aguado, D.S.; Carlberg, R.G.; Côté, P.; González Hernández, J.I.; Lucchesi, R.; et al. The pristine dwarf-galaxy survey—III. Revealing the nature of the Milky Way globular cluster Sagittarius II. *Mon. Not. R. Astron. Soc.* **2021**, *503*, 2754–2762.
114. Fadely, R.; Willman, B.; Geha, M.; Walsh, S.; Muñoz, R.R.; Jerjen, H.; Vargas, L.C.; Da Costa, G.S. Segue 3: An Old, Extremely Low Luminosity Star Cluster in the Milky Way's Halo. *Astron. J.* **2011**, *142*, 88.
115. Fritz, T.K.; Carrera, R.; Battaglia, G.; Taibi, S. Gaia DR 2 and VLT/FLAMES search for new satellites of the LMC. *Astron. Astrophys.* **2019**, *623*, A129.
116. Huxor, A.P.; Mackey, A.D.; Ferguson, A.M.N.; Irwin, M.J.; Martin, N.F.; Tanvir, N.R.; Veljanoski, J.; McConnachie, A.; Fishlock, C.K.; Ibata, R.; et al. The outer halo globular cluster system of M31—I. The final PAndAS catalogue. *Mon. Not. R. Astron. Soc.* **2014**, *442*, 2165–2187.
117. Weisz, D.R.; Dolphin, A.E.; Martin, N.F.; Albers, S.M.; Collins, M.L.M.; Ferguson, A.M.N.; Lewis, G.F.; Mackey, A.D.; McConnachie, A.; Rich, R.M.; et al. A rogues gallery of Andromeda's dwarf galaxies—II. Precise distances to 17 faint satellites. *Mon. Not. R. Astron. Soc.* **2019**, *489*, 763–770.
118. Watkins, L.L.; Evans, N.W.; van de Ven, G. A census of orbital properties of the M31 satellites. *Mon. Not. R. Astron. Soc.* **2013**, *430*, 971–985.
119. Karachentsev, I.D.; Kaisina, E.I.; Makarov, D.I. Suites of Dwarfs around nearby Giant Galaxies. *Astron. J.* **2014**, *147*, 13.
120. Oh, S.H.; Hunter, D.A.; Brinks, E.; Elmegreen, B.G.; Schruba, A.; Walter, F.; Rupen, M.P.; Young, L.M.; Simpson, C.E.; Johnson, M.C.; et al. High-resolution Mass Models of Dwarf Galaxies from LITTLE THINGS. *Astron. J.* **2015**, *149*, 180.
121. Martin, N.F.; Chambers, K.C.; Collins, M.L.M.; Ibata, R.A.; Rich, R.M.; Bell, E.F.; Bernard, E.J.; Ferguson, A.M.N.; Flewelling, H.; Kaiser, N.; et al. Spectroscopy of the Three Distant Andromedan Satellites Cassiopeia III, Lacerta I, and Perseus I. *Astrophys. J.* **2014**, *793*, L14.

122. Richardson, J.C.; Irwin, M.J.; McConnachie, A.W.; Martin, N.F.; Dotter, A.L.; Ferguson, A.M.N.; Ibata, R.A.; Chapman, S.C.; Lewis, G.F.; Tanvir, N.R.; et al. PAndAS' Progeny: Extending the M31 Dwarf Galaxy Cabal. *Astrophys. J.* **2011**, *732*, 76.
123. Martin, N.F.; Ibata, R.A.; Irwin, M.J.; Chapman, S.; Lewis, G.F.; Ferguson, A.M.N.; Tanvir, N.; McConnachie, A.W. Discovery and analysis of three faint dwarf galaxies and a globular cluster in the outer halo of the Andromeda galaxy. *Mon. Not. R. Astron. Soc.* **2006**, *371*, 1983–1991.
124. Sakari, C.M.; Wallerstein, G. The integrated calcium II triplet as a metallicity indicator: comparisons with high-resolution [Fe/H] in M31 globular clusters. *Mon. Not. R. Astron. Soc.* **2016**, *456*, 831–843.
125. Mackey, A.D.; Huxor, A.P.; Martin, N.F.; Ferguson, A.M.N.; Dotter, A.; McConnachie, A.W.; Ibata, R.A.; Irwin, M.J.; Lewis, G.F.; Sakari, C.M.; et al. A Peculiar Faint Satellite in the Remote Outer Halo of M31. *Astrophys. J.* **2013**, *770*, L17.
126. Collins, M.L.M.; Chapman, S.C.; Rich, R.M.; Ibata, R.A.; Martin, N.F.; Irwin, M.J.; Bate, N.F.; Lewis, G.F.; Peñarrubia, J.; Arimoto, N.; et al. A Kinematic Study of the Andromeda Dwarf Spheroidal System. *Astrophys. J.* **2013**, *768*, 172.
127. Alam, S.; Albareti, F.D.; Allende Prieto, C.; Anders, F.; Anderson, S.F.; Anderton, T.; Andrews, B.H.; Armengaud, E.; Aubourg, É.; Bailey, S.; et al. The Eleventh and Twelfth Data Releases of the Sloan Digital Sky Survey: Final Data from SDSS-III. *Astrophys. J.* **2015**, *219*, 12.

Disclaimer/Publisher's Note: The statements, opinions and data contained in all publications are solely those of the individual author(s) and contributor(s) and not of MDPI and/or the editor(s). MDPI and/or the editor(s) disclaim responsibility for any injury to people or property resulting from any ideas, methods, instructions or products referred to in the content.